

POLITECNICO DI TORINO

Facoltà di Mechanical Engineering

Department of Mechanical and Aerospace Engineering

Tesi di Laurea Magistrale

**Experimental investigation of drag  
reduction with riblets in a  
turbulent channel flow**



**Relatori:**

Prof. Gaetano IUSO

Prof. Dr.-Ing. Bettina FROHNAPFEL

Dr.-Ing. Jochen KRIEGSEIS

Dr. Lars VON DEYN

Dr. Marc HEHNER

**Candidato:**

Luigi COPPINI

ANNO ACCADEMICO 2017-2018



# Acknowledgements

*Desidero ringraziare innanzitutto l'Institut für Strömungsmechanik (ISTM) del KIT che mi ha permesso di sviluppare questo progetto di tesi fornendomi supporto teorico e le attrezzature necessarie per le misurazioni sperimentali. In particolare ringrazio la Prof. Dr.-Ing. Bettina Frohnapfel e il Dr.-Ing. Jochen Kriegseis per la disponibilità, l'attenzione e la gentilezza dimostrate durante questo lavoro di tesi, i M. Sc. Lars von Deyn e Marc Hehner per il costante e tempestivo supporto, nonché per la fiducia accordatami con l'accesso al laboratorio.*

*Allo stesso modo ringrazio il professor Gaetano Iuso, relatore di questa tesi presso il Politecnico di Torino, per gli ottimi consigli e per gli insegnamenti forniti.*

*Un doveroso ringraziamento va ai miei genitori, a mia sorella Francesca e a tutta la mia famiglia che mi ha supportato fino alla fine del mio percorso formativo, attraverso un sostegno materiale e intellettuale. La loro completa fiducia nei miei confronti ha contribuito in maniera fondamentale nel mio percorso di crescita e formazione personale. Un ringraziamento speciale a Eleonora, che rappresenta per me un punto di riferimento indispensabile, grazie per aver sempre creduto in me e per avermi sempre offerto il tuo aiuto durante il lavoro di tesi.*

*Infine tutti i miei amici, quelli di vecchia data e quelli con cui ho avuto modo di legare durante questi anni di università e quelli incontrati durante l'esperienza di erasmus, hanno condiviso con me i momenti di felicità e spensieratezza, come anche momenti di fatica e grande impegno. Grazie perché avete riempito di significato il mio percorso di studi magistrali.*



*A mio nonno,  
dal suo esempio ho tratto l'ispirazione e la forza per raggiungere questo traguardo*



# Contents

<b>Acknowledgements</b>	III
<b>1 Introduction</b>	3
<b>2 Experimental setup</b>	5
2.1 Wind tunnel . . . . .	5
2.2 Test section . . . . .	6
2.3 Measurement instrumentation . . . . .	8
2.4 Calibration of the pressure sensors . . . . .	9
<b>3 Uncertainty analysis</b>	13
3.1 Uncertainty estimation with Taylor Series Method . . . . .	14
3.2 Uncertainty of the flow rate measurement . . . . .	15
3.3 Uncertainty of the skin friction coefficient . . . . .	19
<b>4 Reference measurement</b>	23
4.1 Overview of the measurement process . . . . .	23
4.2 Parameters influencing the measurement . . . . .	26
4.2.1 Superficial roughness . . . . .	26
4.2.2 Temperature effects . . . . .	27
4.2.3 Compressibility effects . . . . .	30
4.3 Results . . . . .	32
4.4 Inlet Nozzle . . . . .	34
<b>5 Riblets</b>	37
5.1 Riblets mechanism of drag reduction . . . . .	38
5.2 Results . . . . .	40
5.2.1 Riblet set I . . . . .	41
5.2.2 Riblet set II . . . . .	43
5.2.3 Riblet set III . . . . .	46
<b>6 conclusions</b>	49

A Hot wire measurements	51
Bibliography	55

# List of Tables

3.1	Uncertainty of the measurement variables that define the ambient condition. . . . .	13
3.2	Uncertainty of the adopted pressure sensors. . . . .	14
3.3	UMF of each parameter that influences the Reynolds number. . . . .	16
4.1	Correspondance between orifice diameter and measurable Reynolds number range . . . . .	25
4.2	Measurement timing depending on the orifice diameter . . . . .	30
5.1	Features of the trapezoidal riblets set. The VRC was calculated with the assumption of sawtooth riblets. . . . .	43
5.2	Characteristics of the triangular riblets set with rib spacing $s = 170 \mu m$ . . . . .	45
5.3	Characteristics of the sawtooth riblets set with rib spacing $s = 86 \mu m$ . . . . .	48

# List of Figures

- 2.1 Sketch of the wind tunnel setup with the orifice meter as a device for the flow rate measurement. Colored points, as indicated, refer to the positions of the sensors. The sketch is not to scale, but clearly illustrates the working principle of the facility. . . . . 6
- 2.2 Top view of the test section, from Güttler 2015 [1]. . . . . 7
- 2.3 Cross sectional view of the test section, from Güttler 2015 [1]. . . . . 7
- 2.4 Difference of the pressure measured by the 1 Torr and the 10 Torr full scale Baratron sensors measured at different taps. . . . . 9
- 2.5 Pressure difference between between Setra and Baratron sensors, when measuring the pressure difference between the first and the fifteenth tap at different motor frequencies. The trend of this difference is shown before calibration (a) and after calibration (b). The blue points correspond to the measurements and the red line is the obtained by a linear fit. . . . . 10
- 3.1 Uncertainty of the Reynolds number calculated per each measurement. . . . . 16
- 3.2 Uncertainty in the Reynolds number along the test section, decomposed in the contribution of the different variables. (105 mm orifice) . 17
- 3.3 Distribution of  $Re$  during one measurement and fit to a normal distribution. The total number of collected data points is 6240. The Gaussian distribution is characterized by mean  $\mu = 20022.9$  with a 95% confidence interval  $[20022.4, 20023.3]$  and  $\sigma = 17.45$  with a 95% confidence interval  $[17.15, 17.76]$ . . . . . 18
- 3.4 Random uncertainty of the Reynolds number obtained with a direct calculation from the measurements, with a confidence level of 95%. . 18
- 3.5 Uncertainty in the skin friction coefficient represented as error bands. 20
- 4.1 Pressure drop along the test section, measured with the Baratron sensor. The pressure difference between the 7th tap and the following taps is reported as ordinate and the tap position as abscissa. . . . . 24
- 4.2 Sketch of the adopted orifice meter, taken from [1]. . . . . 25

4.3	Evolution of Reynolds number, temperature and density parameters during the free running time of the wind tunnel. . . . .	29
4.4	Skin friction coefficient is represented for the incompressible approximation (red stars) and when compressible effects are considered (black circles).The measurements at high Re were taken with the 150 mm orifice. . . . .	31
4.5	Variation in the skin friction coefficient considering air compressibility.	31
4.6	Plot of $Re-c_f$ relation separately for the two Plates positions Plate1 and Plate2. The Dean's correlatin is shown with a black dashed line. Filled points correspond to the measurements with exchanged plates.	33
4.7	Plot of $Re-c_f$ relation for the entire test section. Green points correspond to the measurements of the skin friction when the plates position is inverted. . . . .	33
4.8	Skin friction coefficient measured when the inlet nozzle was used for the estimation of the flow rate. . . . .	35
5.1	Vortex visualization in smooth and riblets surfaces at different velocities. (Lee & Lee, 2001 [27]) . . . . .	38
5.2	Longitudinal and crossflow protrusion height. (Bechert et al., 1997 [21]) . . . . .	39
5.3	Protrusion height as a function of the geometry, for different riblets configurations: (a) blade riblets, infinitely thin, (b) blade riblets, blade thickness 2% of lateral rib spacing, (c) parabolic groove profile, (d) triangular riblets (taken from [21]). . . . .	41
5.4	Cross sectional view on trapezoidal riblets manufactured at RWTH Aachen. For additional information refer to [1]. . . . .	42
5.5	Skin friction coefficient measured for the trapezoidal riblets surface, compared with the smooth reference. . . . .	43
5.6	Plot of the wall shear stress difference, for trapezoidal riblets, depending on the riblets Reynolds number. The yellow line is the Bechert correlation in the viscous regime. . . . .	44
5.7	Sketch of the sawtooth shape riblets with spacing $s = 170 \mu m$ , manufactured by 3M. All the dimensions are expressed in $\mu m$ . . . . .	44
5.8	Skin friction coefficient measured for the sawtooth riblets surface with rib spacing $s = 170 \mu m$ compared with the smooth reference. . . . .	45
5.9	Plot of the wall shear stress difference, for sawtooth riblets with spacing $s = 170 \mu m$ , depending on the riblets Reynolds number. The yellow line is the Bechert correlation in the viscous regime. . . . .	46
5.10	Sketch of the sawtooth shape riblets with spacing $s = 86 \mu m$ , manufactured by 3M. All the dimensions are expressed in $\mu m$ . . . . .	47
5.11	Skin friction coefficient measured for thesawtooth riblets surface with rib spacing $s = 86 \mu m$ compared with the smooth reference. . . . .	47

5.12	Plot of the wall shear stress difference, for sawtooth riblets with spacing $s = 86 \mu m$ , depending on the riblets Reynolds number. The yellow line is the Bechert correlation in the viscous regime. . . . .	48
A.1	Plot of the velocity fluctuation component related to the correspondent mean velocity component. . . . .	52
A.2	Flow velocity measurement at different distances from the wall. . . . .	53
A.3	Dimensionless flow velocity as a function of dimensionless wall distance. . . . .	53
A.4	Dimensionless velocity fluctuation as a function of the dimensionless wall distance. . . . .	54





# Chapter 1

## Introduction

In the last decades an intense research activity have been dealing with drag reduction, with the synergy of analytical studies, experimental tests and simulations. One of the most intensively studied solution consists of small surface protrusions aligned with the flow direction, called riblets. Those structures are inspired by nature: the skin of fast-swimming sharks exhibits riblet structures, that reduce the skin friction in the turbulent-flow regime (Dean and Bhushan 2010 [28]).

Numerous researches have investigated the drag reduction mechanism of riblets. Those studies show that riblets cause a modification of the turbulent boundary layer and inhibit the steering phenomenon, with a corresponding reduction in the momentum transfer from the surface. By means of flow visualization techniques (Lee & Lee, 2001 [27]) it was possible to capture images of the flow near the surface: the presence of riblets shifts longitudinal vortices far from the wall, thus reducing the momentum transfer from the rib valleys. In the more recent study of Radmanesh, Mohammadreza, *et al.* [29], flow visualization have evidenced the effect of square riblets on a delta type wing, for low speed configurations, with different angles of attack. The riblets were tested to be effective in reducing the drag force, delaying the flow separation.

Typical values of maximum skin friction drag reduction are in the range 4 – 10% and riblets effectiveness strongly depends on the Reynolds number. When  $Re$  is distant from the design point of the riblets, drag increases due to the increased wetted surface. Several experimental works have proved the effectiveness of riblets in skin friction drag reduction (Walsh 1982 [17]; Bechert *et al.* 1997 [21], Grünenberg & Hage, 2011 [12]). A remarkable contribution was given by Bechert *et al.* 1997 [21], with tests on riblets of various geometries in an oil channel facility, with an accuracy that exceeds all prior air flow investigations. This study demonstrates that the most effective geometry is blade riblets, with a maximum drag reduction of 10%.

Testing in air, compared with oil or water, requires a significant reduction in the physical dimension of riblets, that makes the production of the test surfaces

more expensive and complicated. At the same time air allows to investigate a wider range of Reynolds numbers and to have a longer test length compared to the typical running lengths of oil tunnels. The last property affects the choice of the measurement instrumentation, but does not affect the measure: the drag reduction is independent on the streamwise position (Walsh 1990 [13]).

The present experimental work aims to take highly accurate measurements in a fully developed turbulent air flow and to extend the available data on the change of turbulent skin friction coefficient due to the presence of riblets. The first part of the present work consists of the calibration of the pressure sensors and the setting of the test facility in order to properly take measurements in the range of bulk Reynolds number  $3 \cdot 10^3 < Re_b < 9 \cdot 10^4$  ( $Re_b = U_b H / \nu$ ). Then the study proceeds with measurement of the skin friction coefficient produced by the interaction between the air flow on a smooth surface, that is the reference for the drag reduction calculation. In this phase the effects the most important parameters affecting the measurement are considered and appropriate corrections on the results are operated.

The target of the final part is to perform measurements on three ribletted surfaces and to evaluate the wall shear stress reduction. The results are finally compared with the data present in literature. The study is completed by the uncertainty analysis of the measurement, through the Taylor Series Method.

# Chapter 2

## Experimental setup

This chapter contains all the fundamental details concerning the experimental setup of the wind tunnel based in the Laboratory of the Department for Fluid Mechanics (KIT), that was adopted in the present work. Special attention will be paid on the test section in Section 2.2, on the measurement instrumentation in Section 2.3 and on the critical aspects that will influence the measurement uncertainty analysis of Chapter 3. For more information about the structure and the construction of the wind tunnel the reader can refer to Güttler 2015 [1] and to the bachelor thesis of Jund [2] for the details about the orifice meter.

### 2.1 Wind tunnel

The present experimental work is conducted on the blower wind tunnel specially designed by Güttler with the purpose of measuring small changes of the skin-friction drag with high accuracy. Figure 2.1 illustrates the setup of the facility and the installation positions of the measurement instruments. The air is sucked in the open-circuit system by means of a radial ventilator, controlled by a frequency converter. A flow rate measurement device, that can be an orifice meter or an inlet nozzle, is positioned upstream of the ventilator. The air is subsequently pumped into the backwall of a settling chamber of length 4800 mm and constant inner diameter of 1760 mm. This chamber contains a honeycomb straightener and five stainless steel grids that allow to obtain a symmetric and homogeneous velocity distribution at the outlet, where the test section is positioned. The wind tunnel is designed to produce a fully developed turbulent flow in the shorter length possible. This design goal has been accomplished by applying a tripping of 13% blockage at the inlet of the test section. The flow rate measurement requires a fully developed turbulent flow, therefore tripping is also present at the inlet of the pipe upstream of the orifice meter.

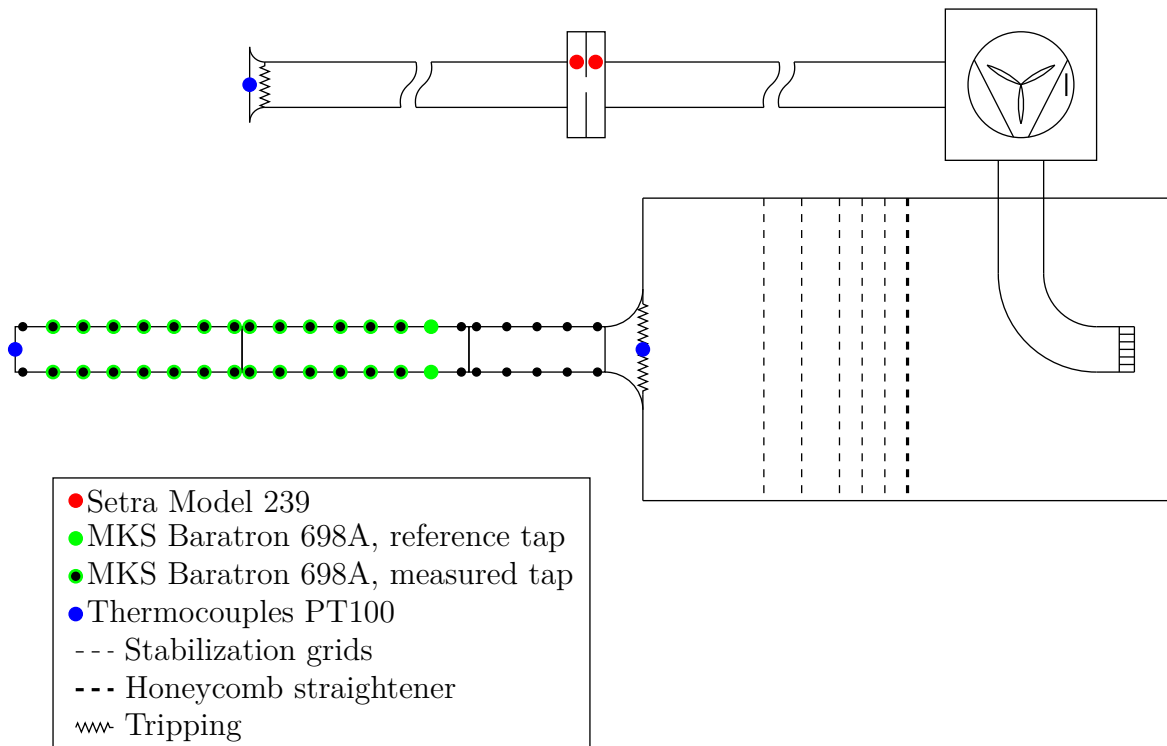


Figure 2.1: Sketch of the wind tunnel setup with the orifice meter as a device for the flow rate measurement. Colored points, as indicated, refer to the positions of the sensors. The sketch is not to scale, but clearly illustrates the working principle of the facility.

The control of the wind tunnel and the data acquisition process are exercised by two PCs through a LabVIEW program. One computer defines the flow rate and for mass continuity, the bulk Reynolds number along the test section, accordingly to the measured ambient conditions. The other is responsible for the measurement of the static pressure drop along the test section.

## 2.2 Test section

The test section is the last part of the wind tunnel encountered by the air flow and is connected to the settling chamber through a fiberglass nozzle of contraction ratio 1:6. An aluminum rounded shape part enhances the rigidity of the connection and reduces disturbances at the test section inlet. The nozzle and the aluminum connection have been accurately manufactured, with a maximum deviation from the design dimensions of 0.02 mm.

The test section presents a rectangular cross section of aspect ratio  $AS = 12$

(height  $H = 25.2$  mm and width 300 mm) and a total length of 3950 mm. The channel is closed by three sets of cast aluminum precision milled cover plates of length 950 mm, 1500 mm and 1500 mm. These plates form the wall of the test section and are characterized by a superficial roughness  $Ra = 0.4 \mu\text{m}$ . The cover plates are screwed to the sidewalls and can be exchanged to conduce experiments on different kinds of surfaces.

The sidewalls consist of two pairs of rods (one pair per each sidewall) of length 950 mm and 3000 mm, cut from the same plate in the direction of grain, to obtain perfectly matching parts with the same height. Figures 2.2 and 2.3 illustrate the above described geometrical features of the test section. Twenty-one pairs of pressure taps, with a diameter of 0.3 mm, are drilled along the sidewalls, orthogonal to the flow direction and centered with respect to the channel height. They are spaced by a constant distance of 200 mm, with exception of the taps located at the intersection between the cover plates, that exhibit 100 mm distance. This allows to detect an eventual misalignment or error in the positioning of the plates, that would lead to a localized pressure drop. Furthermore the first plate is 100 mm distanced from the connection between the nozzle and the test section. Silicon pipes of diameter 0.8 mm connect the pressure taps to the sensor. A leakage-free connection between taps and lines is guaranteed by brass tubes of diameter 0.9 mm, around which the silicon lines are pulled.

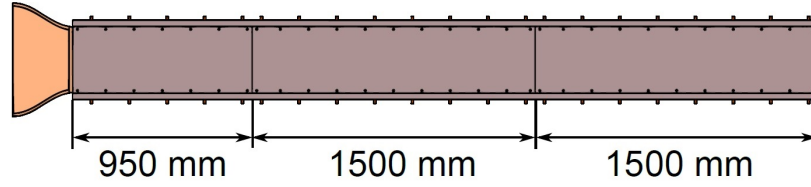


Figure 2.2: Top view of the test section, from Güttler 2015 [1].

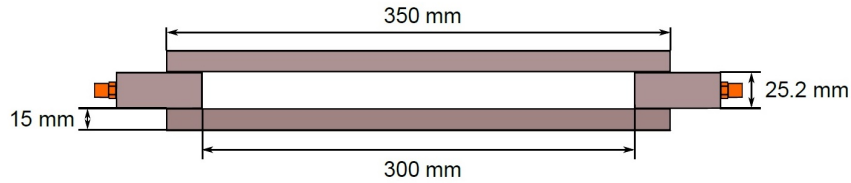


Figure 2.3: Cross sectional view of the test section, from Güttler 2015 [1].

The design solution of taps along the sidewalls suits very well in the case of riblets: taps drilled on the cover plates would have introduced the problem of understanding

if the tap occurs on a riblet tip or valley. This solution is in general favourable when testing a wrinkled surface.

## 2.3 Measurement instrumentation

The experimental setup is equipped with measurement devices that capture the values of the variables involved in the skin-friction coefficient calculation. High accuracy differential pressure transducers measure the flow rate through the wind tunnel and the pressure drop along the test section. A second set of transducers measure the ambient conditions and the temperature at different points of the wind tunnel.

The estimation of the flow rate is based on the measure of the pressure drop between one section upstream and one downstream of the orifice meter (see section ??). This pressure drop is measured by two high-accuracy low-differential pressure transducers Setra Model 239, with different full scale to increase the measurement accuracy.

According to the same principle two high-accuracy differential sensors MKS Baratron 698A with different full scale are used to measure the pressure drop along the test section. These sensors incorporate an inner temperature control housing that keeps the transducer at the constant temperature of 45 °C and allows to minimize the effects of the ambient conditions on the measurement. The output DC signal, coming from the Baratron transducers, is digitized and averaged with two MKS signal conditioners Type 670. The Baratron transducer is used in combination with a Scanivalve multiplexer that allows to connect the desired pressure taps of the test section to the inputs of the pressure sensor.

The ambient conditions strongly affect the reproducibility and accuracy of the measurements, and the final results must be corrected according to the actual values of temperature, ambient pressure and humidity of the air. Three PT100 resistance thermocouples measure the temperature at the inlet, outlet and settling chamber of the test section. A mercury barometer measure the ambient pressure and a Sensirion SHT2 sensor measures the relative humidity of air. The positions of the sensor that measure the parameters of the wind tunnel are shown in Figure 2.1. The transducer that monitor the ambient condition are located in the laboratory at a small distance to the facility.

## 2.4 Calibration of the pressure sensors

The calibration of the pressure sensors, presented in the previous section, enables to combine the electric output signal of the transducers to the value of the pressure that shall be measured. The calibration procedure is as follows: the more accurate MKS Baratron transducers are calibrated first and at a later stage the characteristic curve of the Setra sensors are adjusted on the basis of the characteristic curve of the Baratron. In this preliminary stage, the setup has been modified with the purpose of measuring the same pressure drop with all the pressure sensors. During the calibration of the two Baratron sensors, one input of both sensors was connected to the first tap (fixed as reference) and the other input was connected to one tap per time, starting from the second until the 21<sup>st</sup>. The 60 mm orifice was used for these measurements and the Reynolds number was kept constant at  $Re = 10000$ . From Figure 2.4, that shows the difference between the measurements of the two analyzed sensors, can be observed that the two transducers have different zero and slope of the characteristic lines. The zero error could be easily corrected with a built-in function of the MKS signal conditioner Type 670. The slope error is more difficult to correct and would have required the operation of the company MKS and a long time span incompatible with the duration of this master's thesis project. For this reason the measurements of the pressure drop along the test section were only taken with the most recently calibrated and larger full-scale 10 Torr Baratron sensor.

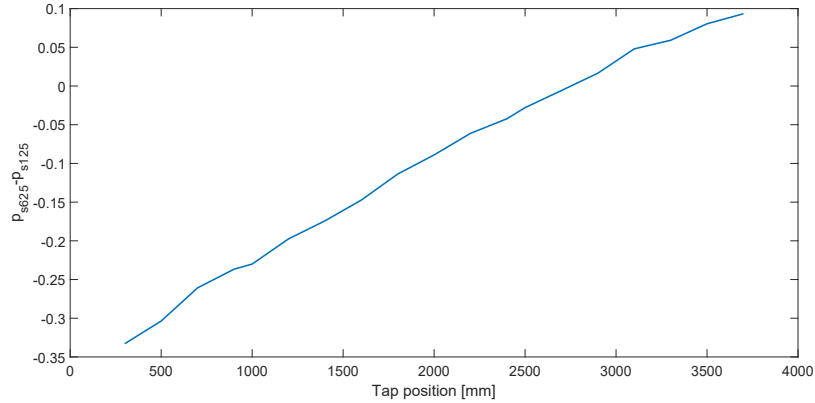
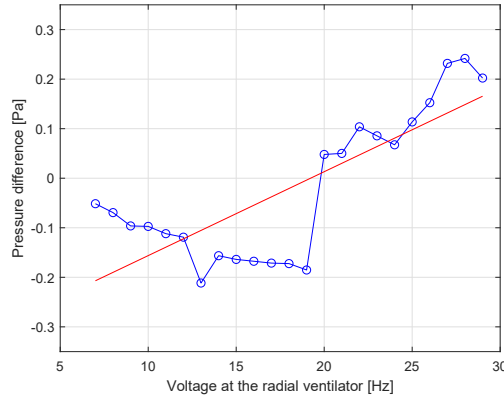


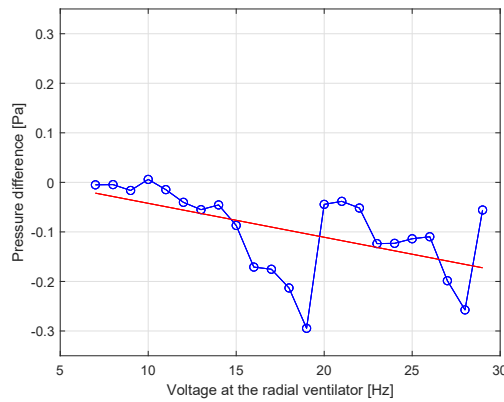
Figure 2.4: Difference of the pressure measured by the 1 Torr and the 10 Torr full scale Baratron sensors measured at different taps.

The calibration of the Setra sensors is carried out connecting their inputs and the inputs of the Baratron sensor with the same pressure difference. The measured quantity, different from the previous case, is the static pressure drop between the first and the 15<sup>th</sup> tap. Twenty-two measures have been taken changing the voltage

at the radial ventilator (from 7V to 29V with steps of 1V), and acquiring different flow rates along the test section.



(a) before calibration



(b) after calibration

Figure 2.5: Pressure difference between between Setra and Baratron sensors, when measuring the pressure difference between the first and the fifteenth tap at different motor frequencies. The trend of this difference is shown before calibration (a) and after calibration (b). The blue points correspond to the measurements and the red line is the obtained by a linear fit.

Figure 2.5 shows the difference between the measurements of the Setra and the Baratron sensor. In this graph the first seven points, associated to lower voltages, correspond to the 125 Pa full-scale Setra sensor and the others to the 625 Pa full-scale transducer. The calibration is conducted introducing two correction coefficients in the variable of LabView program of the pc that controls the wind tunnel. The two coefficients are calculated as the angular coefficient and the zero of the linear regression of the measured set of points. It can be noticed that after the calibration the

zero error is basically eliminated and the slope error is strongly reduced, particularly for the first sensor.

In conclusion the calibration process is performed before the systematic data acquisition campaign and is based on the assumption that the 10 Torr full-scale Baratron sensor is not affected by any error, its characteristic curve can be considered as perfectly coincident with the exact value that needs to be measured. This hypothesis simplifies the calibration of the Setra sensors, that is performed by aligning their characteristic curves to the one of the Baratron sensor. However this assumption will introduce a systematic error in our measurements because the true value is unknown and will never perfectly match with the measured one. Furthermore there will be a correlation between the measurements performed with the Baratron and the Setra sensor, that must be considered during the uncertainty analysis (Chapter 3) of the facility.

The calibration involved also the thermocouples, that were immerse in a biphasic (liquid and solid) mixture of water to set their zero. The value read in the barometer is corrected each time considering the thermal expansion of the mercury.



# Chapter 3

## Uncertainty analysis

The uncertainty analysis of the measurements taken on the wind tunnel is fundamental for the validation of the results. The aim of the present work is to calculate the drag reduction, from the decrease in skin friction coefficient, obtained with a ribletted surface with respect to the reference value of a smooth surface. In order to obtain meaningful results, the error affecting the measurements must be small in comparison to the drag reducing effect. In this Chapter the uncertainty affecting the facility will be theoretically calculated as propagation of the uncertainty of the adopted measurement instruments. In the initial phase of the analysis a general approach has been adopted, that considers the overall error, without dividing it into its systematic and random parts. This approach is used in the first part of the measurements, when the contribution of the single measurement devices in the uncertainty of the result is not exactly defined. The final phase of the uncertainty analysis is more detailed and defines the random part of the uncertainty with a direct calculation from the experimental measurements. The uncertainties of the single measurement devices were read in the datasheets of the instruments or were considered as half of the least scale divisions (or least digit, for a digital measuring instrument). The uncertainties of the instruments measuring the ambient parameters are listed in Table 3.1. Table 3.2 contains the uncertainties of the pressure sensors.

<b>Ambient parameters</b>			
$\delta T [^{\circ}\text{C}]$	$\delta p_{amb} [Pa]$	$\delta h [\%]$	$\delta \rho [m^3/h]$
0.2	30	2	0.13

Table 3.1: Uncertainty of the measurement variables that define the ambient condition.

Pressure sensors	
$\delta p_{Baratron}$	$\delta p_{Setra}$
0.12 of the measurement	0.14 of the full-scale

Table 3.2: Uncertainty of the adopted pressure sensors.

### 3.1 Uncertainty estimation with Taylor Series Method

The Taylor series method (TSM) defines the equation of propagation of the uncertainties of the variables to the uncertainty of the result. This method will be briefly treated here, a more detailed description can be found in Hugh W. Coleman and W. Glenn Steele (2009) [16]. In general, if the result  $r$  is a function of multiple variables:

$$r = f(X_1, X_2, \dots, X_k)$$

the uncertainty of the result can be calculated as a function of the uncertainties of the variables:

$$u_r = \left( \sum_{i=1}^N \left( \frac{\delta r}{\delta X_i} \right)^2 u_{X_i}^2 \right)^{\frac{1}{2}}$$

In this expression the correlation terms are neglected. Those terms are to be introduced when the error sources are not independent. The correlation can be introduced by time-varying effects that affect the error sources of the variables in the same way, or for example they could be caused by an identical systematic error, resulting from the accuracy of the calibration method. For each pair  $(X_i, X_j)$  of variables that share common elemental systematic error sources, an additional term that accounts for the correlated systematic error of the two variables must be introduced as

$$2 \left( \frac{\delta r}{\delta X_i} \right)^2 \left( \frac{\delta r}{\delta X_j} \right)^2 u_{X_i X_j}$$

where  $u_{X_i X_j}$  is the covariance term. The expanded uncertainty of the result  $U_r$  is obtained multiplying the standard uncertainty  $u_r$  by a coverage factor  $k\%$ . For this reason the expanded uncertainty is associated with a given percent level of confidence. The central limit theorem states that if a variable is affected by multiple error sources, then the distribution for this variable will be approximately Gaussian. This allows to use the  $t$  distribution to calculate the expanded uncertainty.

$$U_r = t\% u_r$$

The error propagation equation can be expressed in nondimensionalized form as

$$\frac{U_r^2}{r^2} = \left( \sum_{i=1}^N \left( \frac{X_i}{r} \frac{\delta r}{\delta X_i} \right)^2 \left( \frac{U_{X_i}}{X_i} \right)^2 \right)$$

This expression is useful to define a parameter that defines the role of the uncertainties of one variable in the uncertainty of the final result. The uncertainty magnification factors (*UMF*) are defined as

$$UMF_i = \frac{X_i}{r} \frac{\delta r}{\delta X_i}$$

If the  $UMF_i > 1$  it indicates that the uncertainty of the variable  $X_i$  is magnified as it propagates to the result, vice versa, the influence of the uncertainty in the variable  $X_i$  is diminished as it propagates to the result when  $UMF_i < 1$ . The last parameter that will be used in the uncertainty analysis is the uncertainty percentage contribution (*UPC*), defined as

$$UPC_i = \frac{\left( \frac{\delta r}{\delta X_i} \right)^2 (U_{X_i})^2}{U_r^2} \cdot 100$$

that gives the percentage of the contribution of the uncertainty in the variable to the uncertainty of the result.

## 3.2 Uncertainty of the flow rate measurement

A description of the measurement of the mass flow rate running through the wind tunnel is provided in Section 4.1. In this case, the final parameter resulting from the flow rate measurement with the orifice meter is the Reynolds number of the flow in the test section

$$Re = \frac{U_b H}{\nu}$$

where  $H$  is the height of the test section,  $\nu$  is the kinematic viscosity at the outlet of the facility and the bulk velocity  $U_b$  is obtained dividing the volume flow rate by the cross sectional area of the test section.

The uncertainty in the mass flow rate measurement is calculated applying the formula provided in the norms DIN EN ISO 5167-1 [18] and DIN EN ISO 5167-2 [19]:

$$\frac{\delta q_m}{q_m} = \sqrt{\left( \frac{\delta C}{C} \right)^2 + \left( \frac{\delta \epsilon}{\epsilon} \right)^2 + \left( \frac{2\beta^4}{1-\beta^4} \right)^2 \left( \frac{\delta D}{D} \right)^2 + \left( \frac{2}{1-\beta^4} \right)^2 \left( \frac{\delta d}{d} \right)^2 + \frac{1}{4} \left( \frac{\delta \Delta p}{\Delta p} \right)^2 + \frac{1}{4} \left( \frac{\delta \rho_{in}}{\rho_{in}} \right)^2}$$

On the basis of the uncertainty in the mass flow rate it is possible to apply the TSM and find the uncertainty in the Reynolds number. The results of this procedure are reported in Figure 3.1, for each of the three orifices exploited during the measurements. The uncertainty values are calculated considering the ambient conditions in the moment of the measurement.

Similar results are obtained applying the TSM for the entire calculation of the uncertainty in the Reynolds number of the test section. This method is useful to understand the connection between the uncertainty of the parameters and the uncertainty of the results, as introduced in the previous section. Table 3.3 contains the UMF of each parameter influencing the final result. The UPC quantifies the percentage of influence of each variable in the Reynolds number. A visual representation of the UPC, for the intermediate orifice, can be observed in Figure 3.2. The different colors indicate measurements with orifices of different inner diameter. The uncertainty depends on the ambient condition in the moment of the measurement.

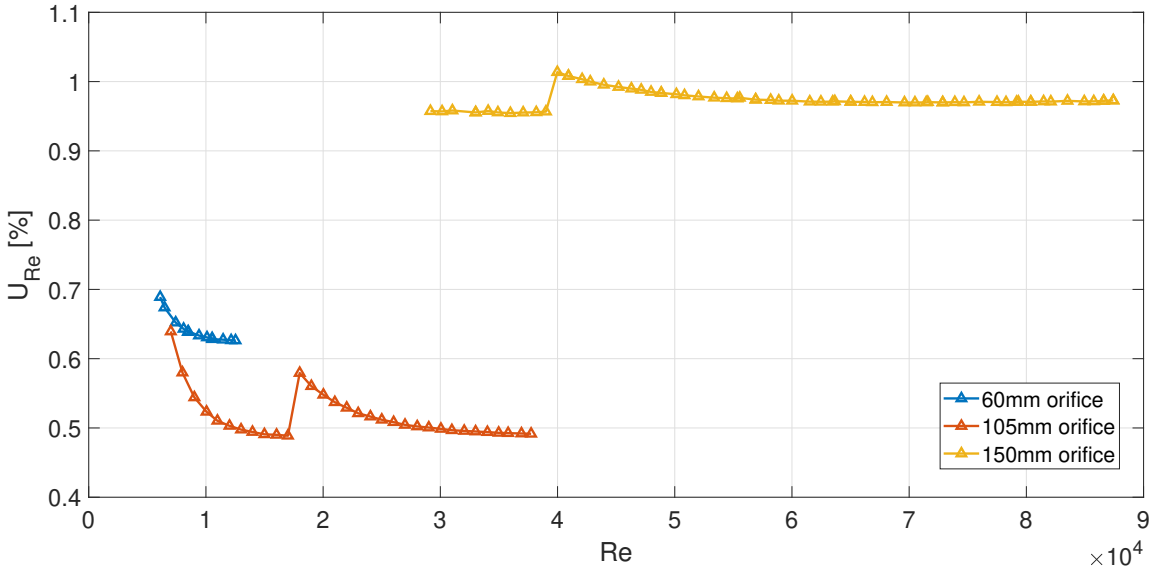


Figure 3.1: Uncertainty of the Reynolds number calculated per each measurement.

parameter	C	e	d	$\Delta p$	$\rho_{in}$	$\beta = 0.6$	$\beta = 0.525$	$\beta = 0.75$	l	$\nu$
UMF	1	1	2	0.5	0.5	0.596	0.329	1.851	1	1

Table 3.3: UMF of each parameter that influences the Reynolds number.

At this point it is interesting to compare the uncertainty estimation of the TSM with a direct calculation from the experimentally measured data. The Reynolds

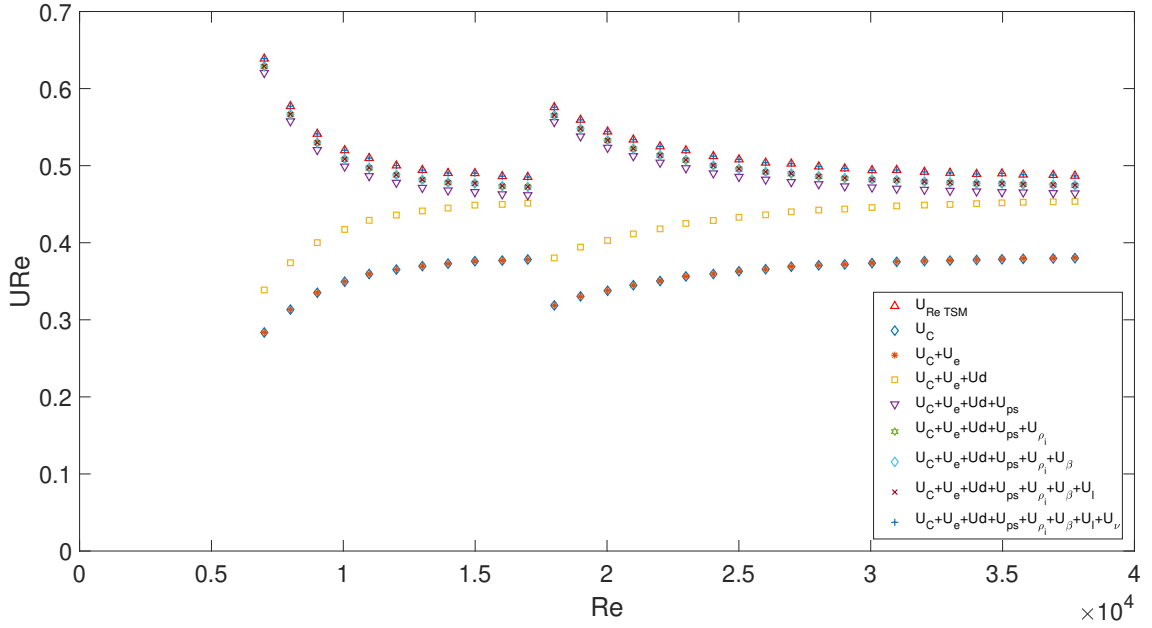


Figure 3.2: Uncertainty in the Reynolds number along the test section, decomposed in the contribution of the different variables. (105 mm orifice)

number distribution is firstly considered. The histogram in Figure 3.3 contains the distribution of the Reynolds number corresponding to the measurement with average value  $Re = 20022.9$ , together with the fitting of the normal distribution. As expected from the central limit theorem, the collected data present a good match with the Gaussian distribution.

Proceeding deeper with the analysis, the random component of the Reynolds number's uncertainty can be directly calculated as

$$s_{Re_{DIRECT}} = \sqrt{\frac{1}{N-1} \sum_{i=1}^N (Re_i - \overline{Re})^2}$$

A coverage factor  $t = 2$  is adopted to calculate the random uncertainty with a confidence level of 95%. The results obtained with this procedure are reported in Figure 3.4. Comparing the results it is possible to observe that the uncertainty calculated with the TSM method is higher with respect to the one obtained with the direct calculation. This is both attributable to the fact that the direct calculation does not take into account the systematic uncertainty and to the fact that, in this analysis, the covariance terms have been neglected in the uncertainty calculated with the TSM.

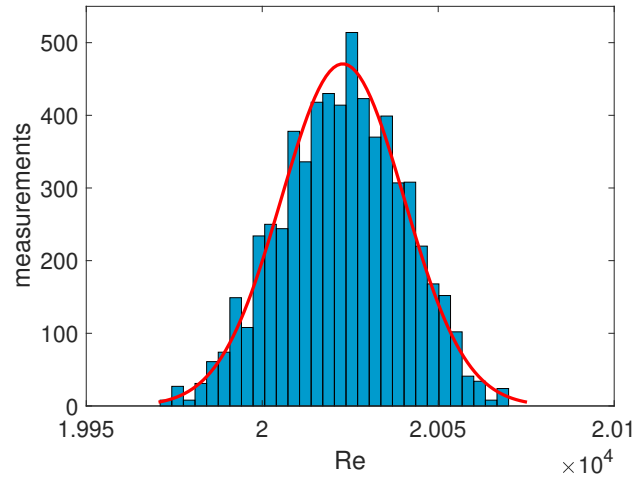


Figure 3.3: Distribution of  $Re$  during one measurement and fit to a normal distribution. The total number of collected data points is 6240. The Gaussian distribution is characterized by mean  $\mu = 20022.9$  with a 95% confidence interval  $[20022.4, 20023.3]$  and  $\sigma = 17.45$  with a 95% confidence interval  $[17.15, 17.76]$ .

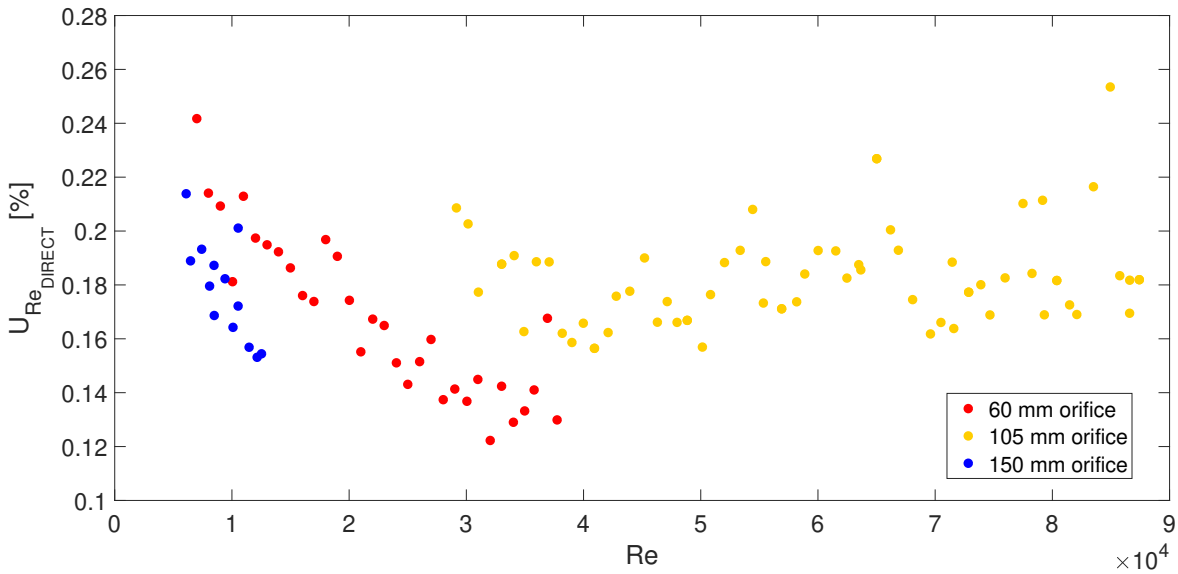


Figure 3.4: Random uncertainty of the Reynolds number obtained with a direct calculation from the measurements, with a confidence level of 95%.

### 3.3 Uncertainty of the skin friction coefficient

The final step of the uncertainty analysis is the calculation of the uncertainty that affects the skin friction coefficient  $c_f$ . The TSM is adopted to combine the measurement uncertainty of the flow rate, calculated in section 3.2, and the uncertainty of the static pressure measurements along taps of the test section. A brief description of the skin friction measurement process is outlined in Section 4.1. Three main error sources can be identified for this parameters:

- Uncertainty in the flow rate measurement
- Uncertainty of the Baratron pressure sensor
- Uncertainty in the tap position and orientation with respect to the air flow

Considering solely the test section, it is possible to focus on the uncertainty of the wall shear stress  $\tau_w$ . It is initially assumed that the uncertainty of the pressure measurement is bigger than the uncertainty of the tap's position, so that the last one can be neglected. The uncertainty in the  $\tau_w$  is directly correlated with the uncertainty of the Baratron pressure sensor, that is 0.12% of the measurement. For this reason the pressure uncertainty changes in different taps of the test section, due to the pressure gradient introduced by the flow. As a consequence the uncertainty of the wall shear stress is calculated for the normalized linear regression of the pressure difference along the test section, characterized by a constant error band. The expression for the standard deviation of the normalized linear regression is:

$$\sigma_{lr} = \sqrt{\frac{\sum_{i=1}^N \left( \frac{\Delta p_i}{a_i x - b_i} - 1 \right)^2}{N - 2}}$$

where  $\Delta p_i$  is the pressure drop of the  $i^{th}$  tap with respect to the reference,  $a_i$  and  $b_i$  are the coefficients of the linear regression,  $x$  is the position of the  $i^{th}$  tap with respect to the reference,  $N$  is the number of considered taps. This quantity is nearly constant  $\sigma_{lr} = 0.0013$  in the considered range of  $Re$ , that is one order of magnitude higher than the pressure sensor uncertainty. With a more careful observation of the experimental data it is possible to detect a systematic shift of the measured pressure drop points with respect to the linear regression. This is clearly due to the error in the positioning and in the direction of the tap. Even a small error in this parameter could cause a systematic deviation, with respect to the real value, that is higher than the uncertainty of the pressure sensor. This error could be easily corrected with a measurement of the distance between the inlet of the test section and the position of each tap, but it was not possible to detect the positioning error with the measurement instruments present in the laboratory, characterized by an uncertainty

of 1 mm. Additionally it is not possible to correct the data in the post processing, because none of the taps can be a priori assumed as correctly positioned.

In the present analysis the error in the taps positioning is considered in the systematic uncertainty that characterizes the linear regression.

The uncertainty of the skin friction coefficient is calculated by applying the TSM, considering the error propagation of the flow rate measurement and of the static pressure drop measurement. In Figure 3.5 are visualized the uncertainty of  $c_f$  as error bands. The three bands in the graph correspond to the orifice used for the measurement. Furthermore, the bands are centered with respect to the curve that fits the measured points.

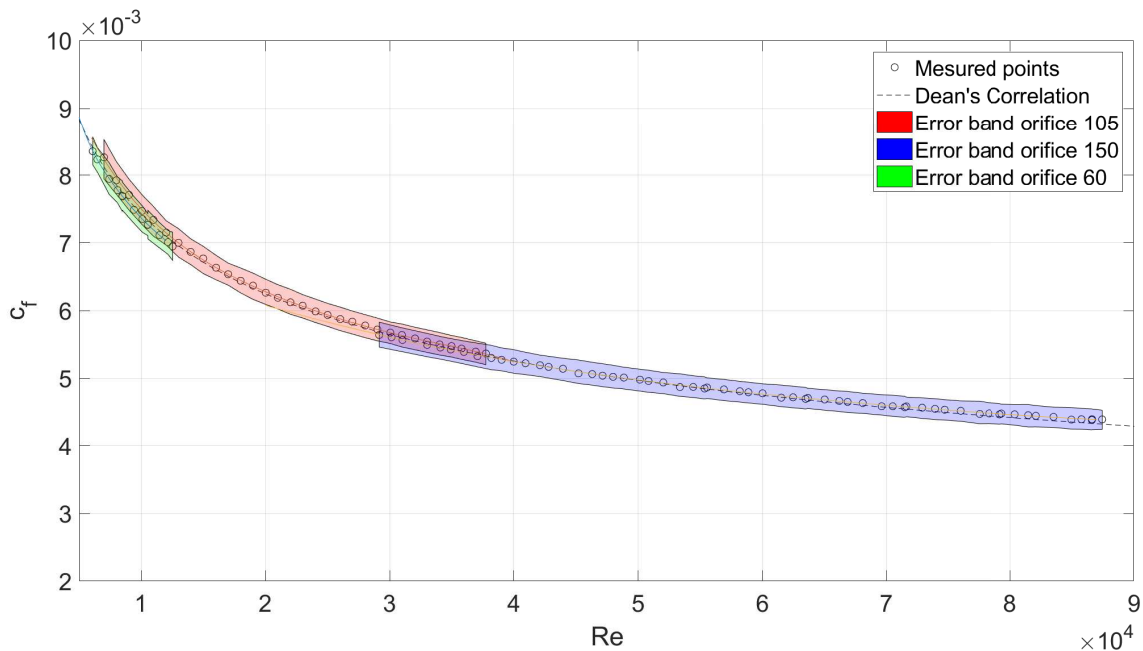


Figure 3.5: Uncertainty in the skin friction coefficient represented as error bands.

Finally the reproducibility of the measured points must be analyzed. An optimal approach could be to select some values of Reynolds numbers in the range of the present study and to test the skin friction in different times, with different ambient condition. The comparison between this measurements and the uncertainties calculated with the TSM would give an experimental validation of the results shown above. However it is difficult to set the Reynolds number at the same value with different ambient conditions, because the parameter controlling the flow rate through the wind tunnel is the radial ventilator frequency. An alternative, but equivalently effective, method have been followed in the present work: the experimental analysis of the reproducibility was obtained comparing the points of the fitting curves

of the points, with a sufficiently long time intercurring between the measurements, in order to eliminate the problem of the Reynolds number tuning. This method was applied to the measurements conducted with the 150 mm orifice, considering the measurements distributed as a normal distribution. Imposing a confidence interval of 99%, the maximum uncertainty obtained was  $3.5 \cdot 10^{-5}$ , lower with respect to the uncertainty calculated with the TSM. This result could have been predicted from Figure 3.5, where the measurements are positioned in the central part of the error band. In conclusion, the uncertainty band calculated with TSM is more conservative than the the one experimentally calculated.



# Chapter 4

## Reference measurement

The aim of this Chapter is to report the results from the measurements of a smooth surface in the test section, for a fully developed turbulent channel flow. The transition to turbulence at low Re is accomplished through artificial tripping. The results from the smooth surface will be compared with literature data and will be used as a reference in Chapter 5. In previous works similar measurements were already taken: the smooth reference must be updated to consider eventual changes in the calibration of the measurement devices and other possible changes of the system. Additionally this is the first time that the orifice meter is used as unique device for measurement of the flow rate: in previous measurement campaigns it was used in combination with the inlet nozzle. In the first part of the Chapter, the measurement process and the calculation of the wall shear stress  $\tau_w$  and the wall skin friction coefficient  $c_f$  are briefly explained. Secondly the effects on the measurement of superficial roughness of the test section walls, temperature and compressibility are considered. The measurement timing and the calculations will be properly adapted to include this effects. Finally the results from the smooth surface will be shown and compared with the results obtained exchanging the plates of the test section, characterized by different superficial roughness.

### 4.1 Overview of the measurement process

The calculation of the skin friction coefficient  $c_f$ , characteristic of the surface interacting with the channel flow, is performed starting from the measurement of the pressure drop along the test section. The static pressure is consecutively measured in the desired taps and the pressure  $\frac{dp}{dx}$  drop is derived as the angular coefficient of the linear regression of the measured points (see Figure 4.2).

Scaling the pressure drop with the characteristic length of the test section  $\frac{H}{2}$  (the distance between the upper or lower walls and the centerline) it is possible to

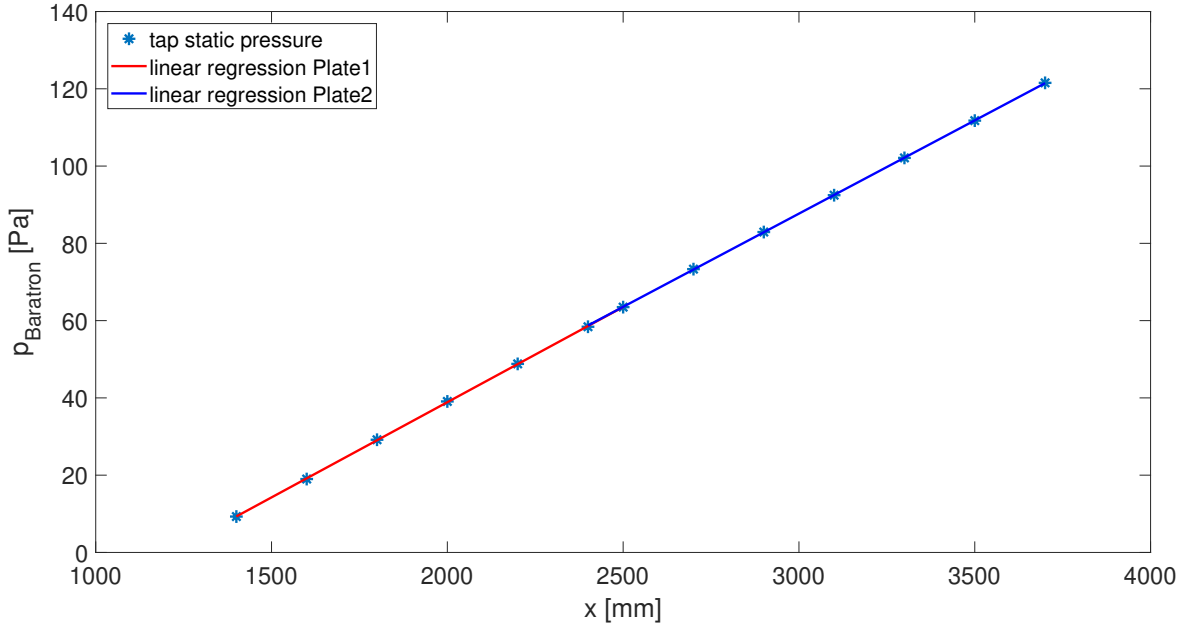


Figure 4.1: Pressure drop along the test section, measured with the Baratron sensor. The pressure difference between the 7th tap and the following taps is reported as ordinate and the tap position as abscissa.

calculate the wall shear stress  $\tau_w$ .

$$\tau_w = \frac{dp}{dx} \frac{H}{2}$$

Finally the skin friction coefficient  $c_f$  can be computed with the following formula:

$$c_f = \frac{\tau_w}{\frac{1}{2}\rho U_b^2}$$

where  $\rho$  is the density of air at the outlet of the test section and  $U_b$  is the bulk velocity of the flow along the test section. This velocity is computed considering the mass continuity in every part of the wind tunnel (neglecting leakages) and exploiting the measurement of the flow rate performed with an orifice meter positioned in the inlet pipe (see Figure 2.1). The orifice is a sudden narrowing of the diameter of the pipe. The flow passing through the orifice generates a pressure difference between a section upstream and downstream the orifice plate. DIN EN ISO 5167 contains the design guidelines for this flow meter and the empiric correlations between the volumetric flow rate  $\dot{V}$  and the pressure drop  $\Delta p$ . The parameter  $\beta$  is the ratio between the diameter of the orifice plate  $d$  and the diameter of the inlet pipe  $D$ ,

the parameters  $A$  and  $C$  are functions of the Reynolds number  $Re_D$ , based on the inlet-pipe diameter  $D$ . Consequently the calculation of the flow rate is performed exploiting an iterative algorithm, with initial parameters suggested by the norm.

$$\dot{V} = \frac{C}{\sqrt{1-\beta^4}} e^{\frac{\pi}{4}} \sqrt{\frac{2\Delta p}{\rho_{in}}}$$

$$\beta = \frac{d}{D}$$

$$A = \left(\frac{1900\beta}{Re_D}\right)^{0.8}$$

$$C = 0.5961 + 0.0261\beta^2 - 0.216\beta^8 + 0.000521\left(\frac{10^6\beta}{Re_D}\right)^{0.7} + (0.0188 + 0.0063A)\beta^{3.5}\left(\frac{10^6\beta}{Re_D}\right)^{0.3}$$

The influence of the ambient conditions on the flow rate computation are taken into account (see [1]). Different values of the parameter  $\beta$  allow to measure a bigger range of flow rates, given the full-scale of the sensor adopted to measure  $\Delta p$ . The correspondence between orifice diameter and the  $Re$  range is collected in Table 4.1

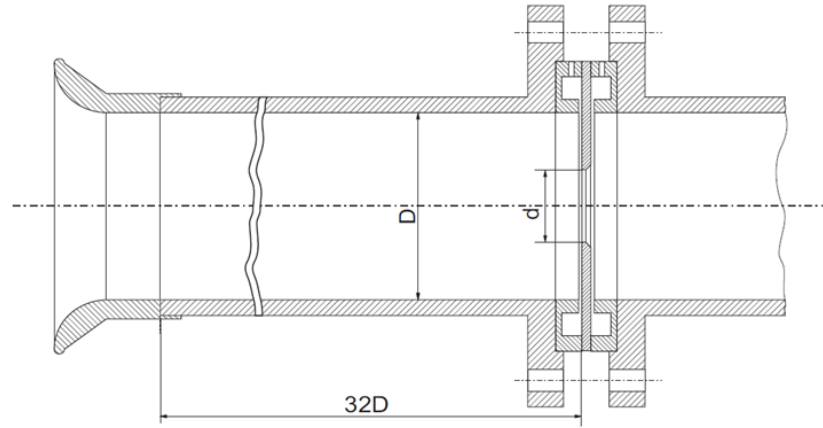


Figure 4.2: Sketch of the adopted orifice meter, taken from [1].

$d$ [mm]	60	105	150
$Re$	7000 – 12000	10000 – 38000	28000 – 87000

Table 4.1: Correspondance between orifice diameter and measurable Reynolds number range

In conclusion, this measurement process makes possible to calculate the skin friction coefficient of the two plates separately or the one of the entire test section,

just by selecting the proper taps. It is also possible to conduct measurements with different surfaces exchanging the plates of the test section.

## 4.2 Parameters influencing the measurement

This Section presents the parameters that condition the measurement process. The effects of the ambient conditions were already discussed in [1]. First the superficial roughness for the smooth reference was an open topic that will be solved with the experiments carried out in this study. Secondly the temperature effects are considered to set the proper measurement timing. Finally the effects of air compressibility are calculated, in particular for high flow rates.

### 4.2.1 Superficial roughness

The measurement of a smooth reference would imply to expose the flow to a surface characterized by no roughness. This surface can not be obtained in reality and a maximum acceptable roughness must be defined for the smooth surface. In this Section the most significant literature connected to the influence of wall roughness on the flow properties will be presented and exploited to understand the conducted experiments. The surface roughness can be indirectly measured considering the change in the flow characteristics. If the wall roughness is increased, the friction coefficient  $c_f$  is enhanced for corresponding values of  $Re$ . The logarithmic layer is also affected and shifted downward. By varying the Reynolds number it is possible to observe three turbulent flow regimes: hydraulically smooth, rough transitional and fully rough.

Historically, Nikuradse (1933) [5] performed the first tests on rough surfaces obtained by sand grains cemented to the walls. Subsequent articles frequently adopt as a standard parameter the Nikuradse equivalent roughness  $k_s$ . In the same period Colebrook & White (1937) [6] found a monotonic behavior of roughness function and their results were used by Moody (1944) [7] to create the famous diagram. Bradshaw (2000) [8] arose the question if the roughness gets relevant over a certain Reynolds number. In particular contrasting studies were produced regarding the Townsend hypothesis. It was introduced by Townsend (1976) [9] and stated that if the roughness height  $k$  is small compared to the characteristic length  $D$ , the turbulent structure in the outer-layer is similar over smooth and rough walls, meaning that in this region the mean velocity and the turbulence intensity are unaffected by the wall roughness. This law is valid outside the roughness sublayer, that is the area where the flow parameters are influenced by the wall roughness. The outer-layer is defined as the part of the flow with a distance of  $5k$  or bigger from the wall. Jiménez (2004) [14] proposed that the outer flow is not affected by wall roughness

if the lengthscale of the roughness height  $k$  is small compared to the lengthscale of the boundary layer thickness  $\delta$ , in particular if  $\frac{k}{\delta} < \frac{1}{50}$ . The outer layer similarity and the criterion of Jiménez were confirmed by J.J. Allen et al. (2007) [10], that conducted tests with honed pipes in the Princeton superpipe facility. An equivalent Nikuradse sand-grain roughness  $k_s = 3.0k_{rms}$  presented hydraulically smooth behaviour for  $Re_D < 27 \cdot 10^6$ . Similar results were obtained by Schultz (2006) [11] testing surfaces characterized by a 3D roughness with nearly Gaussian distribution.

Previous experiments with plates of different superficial roughness were conducted on the same facility. The results of those measurements showed that the skin friction coefficient is strongly affected by the wall roughness variation. However those experiments analyzed a reduced number of taps for the calculation of the parameters of interest. In the experiments of the present study the same set of plates are tested. The first set presents a superficial roughness  $Ra = 0.4\mu m$ , the second set was further polished to obtain a smoother wall surface. The plates are tested in exchanged position, to understand if the difference in skin friction coefficient is caused by the roughness variation or by a systematic error typical of the facility. The results (Section 4.3) comparability is guaranteed, because the plates are placed simultaneously along the test section.

## 4.2.2 Temperature effects

The temperature of the fluid is constantly monitored during the experiments by means of thermocouples (see Figure 2.1), because it strongly affects the acquired data. The temperature at the inlet and at the outlet of the wind tunnel are parameters that affect respectively the calculation of the flow rate and of the skin friction coefficient. In general, a temperature change causes a variation of the density and of the viscosity in the flow. The heating sources present in the wind tunnel are mainly two: the heating due to the rotation of mechanical parts in the radial ventilator and the heat created by turbulent dissipative effects in the radial ventilator and along the test section, where the flow velocity is high. Those thermal effects can be controlled by selecting the proper timing for the different steps of the measuring process. The measurement of the static pressure in different taps of the test section is not simultaneous, but it is sequentially taken, starting from the analyzed tap closer to the inlet, to the one closer to the outlet of the test section. This procedure of data acquisition allows to have easier calculations, using the average temperature, only if the temperature variation is small during the measurements in the entire set of considered taps. In order to have small temperature changes during the experiments, the heating effects must be controlled selecting proper values for three important parameters: the free running time of the tunnel, that is, the time between the switch on of the radial ventilator and the starting of the measurements, the time needed for one measurement at a defined flow rate and the time between

two measurements at different flow rates. A correct setting of this parameters allows to have a maximum variation of the temperature at the outlet of the test section  $T_{outlet}$  of 0,6 °C during one measurement.

Furthermore the heating effects along the test section caused by the turbulent motion must be monitored. For this purpose the difference  $T_{outlet} - T_{inlet}$  between the temperatures at the inlet and the outlet of the test section must be monitored and kept as small as possible, otherwise the temperature gradient would affect the static pressure in different taps.

Figure 4.3 shows the evolution of parameter of interest during a free running time of two hours. Graphs (c) and (d) report the density and the temperature at the inlet, while graphs (e) and (f) show the same parameters at the outlet of the wind tunnel. As expected, these two parameter have opposite behaviour and at the outlet converge to a fixed value after around one hour. A similar behaviour is followed by the temperature inside the settling chamber and by the Reynolds number of the flow inside the test section. For this reason, the free running time was set to one hour for each measurement of the campaign. Finally, the temperature at the inlet is connected to the room temperature and is not visibly affected by the thermal phenomena of the wind tunnel. An air conditioning system in the laboratory would help to have a constant  $T_{inlet}$ .

Table 4.2 contains the time parameters adopted during the measurement campaigns for the smooth and the ribletted surface. This parameters were selected with the purpose of minimizing the thermal effect caused by the air flow running into the system. With larger orifice diameters it is possible to conduct experiments at higher Reynolds number. The higher flow rate introduces stronger thermal effects and the measuring times must be reduced, compatibly with the necessity of acquire a sufficient number of pressure data for the averaging process. On the contrary, for high flow rates the time between measurements at high Reynolds number is increased because the thermal equilibrium is reached in a longer time. The time between taps is also increased in order to consider that the larger pressure gradient along the test section requires more time for the pressure sensor to stabilize.

Regarding the desired timing and to make the process more automatic, some small modification was applied to the LabVIEW program controlling the measurement: when, for a given Reynolds number, the measurement of the static pressure is completed in all the taps, the frequency at the radial ventilator is automatically changed to the value correspondent to the next  $Re$  to be tested and the measurement process starts considering the same timing of the previous measurement. This allows to save time and to increase the repeatability of the measurement.

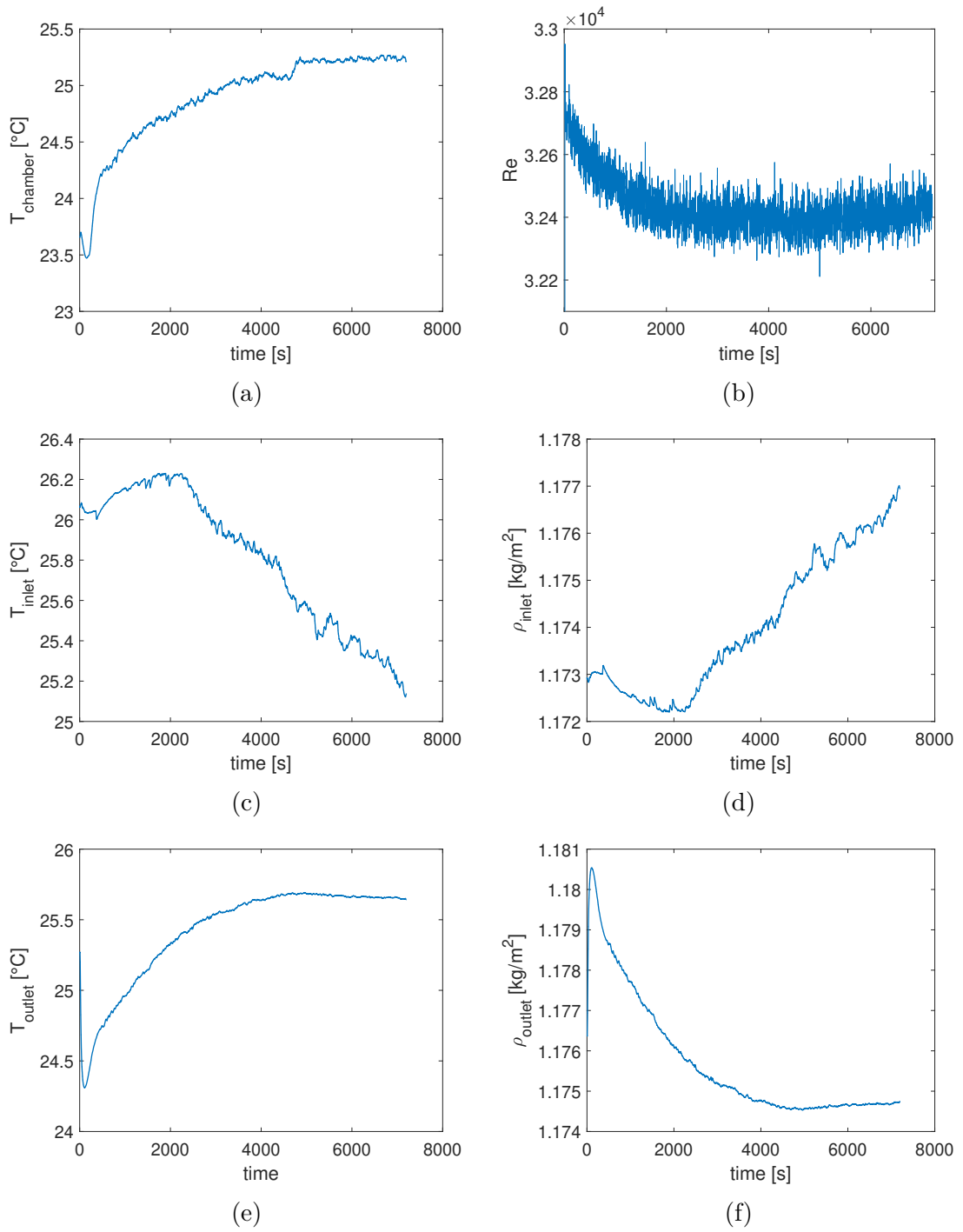


Figure 4.3: Evolution of Reynolds number, temperature and density parameters during the free running time of the wind tunnel.

Orifice diameter [mm]	Free running time [min]	Measurement time [s]	Time between taps [s]	Time between measurements [min]
60	60	120	30	10
105	60	60	30	10
150	60	30	40	15

Table 4.2: Measurement timing depending on the orifice diameter

### 4.2.3 Compressibility effects

Another important aspect that must be considered is the compressibility of air at high Reynolds numbers. The maximum Reynolds number tested during the measurement campaign (see Chapter 4) was  $Re_{max} = 87400$  corresponding to  $Ma_{max} = 0.165$ . The approximation to incompressible flow for  $Ma < 0.2$  is commonly adopted. Nevertheless, neglecting this effect, the high accuracy of the measurements would be associated with a systematic error that scales proportionally to the flow velocity. The compressibility due to the flow acceleration can be taken into account expressing the ratio between the total density  $\rho_t$  and the static density  $\rho$  of the flow as a function of the Mach number.

$$\frac{\rho_t}{\rho} = \left(1 + \frac{\gamma - 1}{2} Ma^2\right)^{\frac{1}{\gamma - 1}}$$

where

$$Ma = \frac{v}{c_s} \quad \gamma = 1.4$$

The speed of sound  $c_s$  in humid air is calculated according to O. Cramer [3], depending on the Saturation vapor pressure defined by R. S. Davis [4]. This calculation is based on the actual values of ambient pressure, temperature and relative humidity measured simultaneously with the skin friction coefficient. Figure 4.4 shows the results, measured with the orifice of diameter 150 mm, when compressibility effects are neglected (red stars) and when they are considered (black circles). The variation between these two sets of points is proportional with the Reynolds number as can be observed in Figure 4.5. If the compressibility effects are considered, the measured points present a better agreement with the Dean's correlation.

The biggest registered variation in the  $c_f$  when these effects are taken into account is  $-1.3\%$ , as can be observed in Figure 4.5. From this analysis it can be concluded that the compressibility effects must be considered, in particular when the mean velocity of the flow is high. Previous experiments, with high flow velocities, were conducted on the same facility: the results showed, in the range of for high  $Re$ , correspondingly higher values of the skin friction coefficient. This measurements

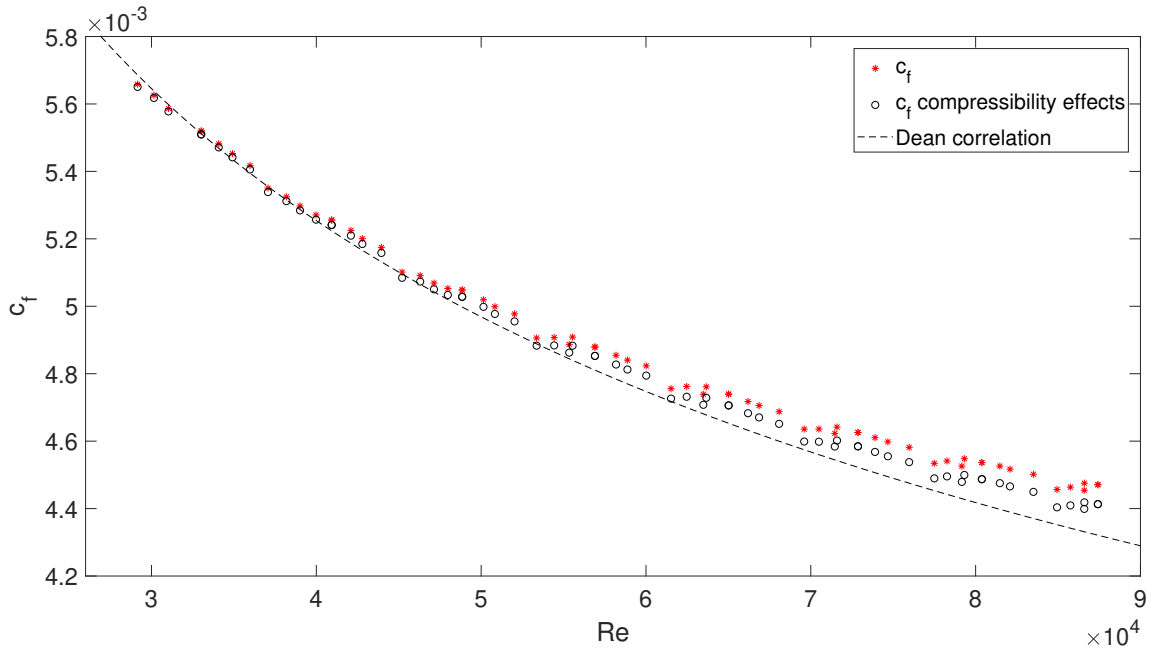


Figure 4.4: Skin friction coefficient is represented for the incompressible approximation (red stars) and when compressible effects are considered (black circles). The measurements at high  $Re$  were taken with the 150 mm orifice.

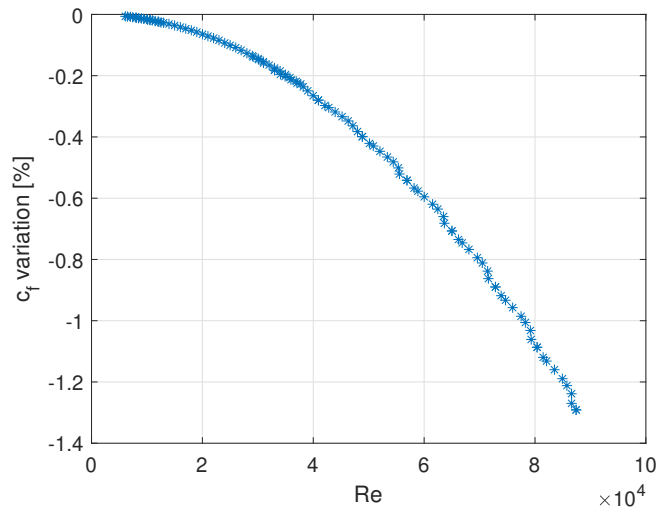


Figure 4.5: Variation in the skin friction coefficient considering air compressibility.

are probably affected by a systematic error introduced with the incompressibility hypothesis.

### 4.3 Results

In this sections the results of the measurement campaign for the smooth plates are shown and commented. The calculation of the skin friction coefficient, performed with Matlab, takes into account the effects of the parameters presented in Section 4.2. During this campaign the exploited taps range from the 8<sup>th</sup> to the 20<sup>th</sup> (see Figure 4.2). The reference tap is moved to the 7<sup>th</sup> position, limiting the number of available taps for the measurement, in order to avoid that the full-scale of the pressure sensors is exceeded. The last tap is close to the test section's outlet and could be affected by the exit of the flow, therefore it is not considered. The results will be compared with the correlation proposed by Dean (1978) [15], obtained with the interpolation of data coming from different sources and facilities:

$$c_f = 0.073Re^{(-0.25)}$$

As already introduced in Section 4.2.1, the plates tested in the smooth measurements exhibit different superficial roughness: one set has roughness  $Ra = 0.4\mu m$ , the other has been further polished to obtain a lower roughness.

Figure 4.6 shows the  $Re - c_f$  behavior separately for the two plates sets. In this case the plates set with higher roughness is placed in position Plate1, situated closer to the test section inlet, the plates set with lower roughness is in position Plate2. The three orifices exploited for the flow rate measurement during the campaign can be clearly recognized. Vertical gaps are present in the range of shift to an orifice with different diameter. The ranges of Reynold number where the orifices work properly, depend on the orifice diameter and are collected in Table 4.1.

Additionally, the results present a shift, almost constant, between the skin friction coefficients of the two plates: the plates with lower roughness shows a lower  $c_f$ . The causes of this shift were subject of debate of previous experiments on the wind tunnel and they were not completely recognized. The shift could be attributed to a drag reduction caused by the lower roughness or to a systematic error of the facility, caused by the error in the positions of the taps. Consequently, the plates have been exchanged of position to better understand the causes of this vertical shift. 8 points at 4 flow rates were measured in different days (with different ambient conditions), with the orifice of diameter  $d=150mm$ . This orifice allows to reach higher flow rates and Reynolds number, where the boundary layer thickness is reduced and the shift of  $c_f$  is more likely to happen. The results obtained exchanging the plates are visible in the same plot as filled points. There is an evident matching with the results obtained in the previous configuration. This evidences that the variation of superficial

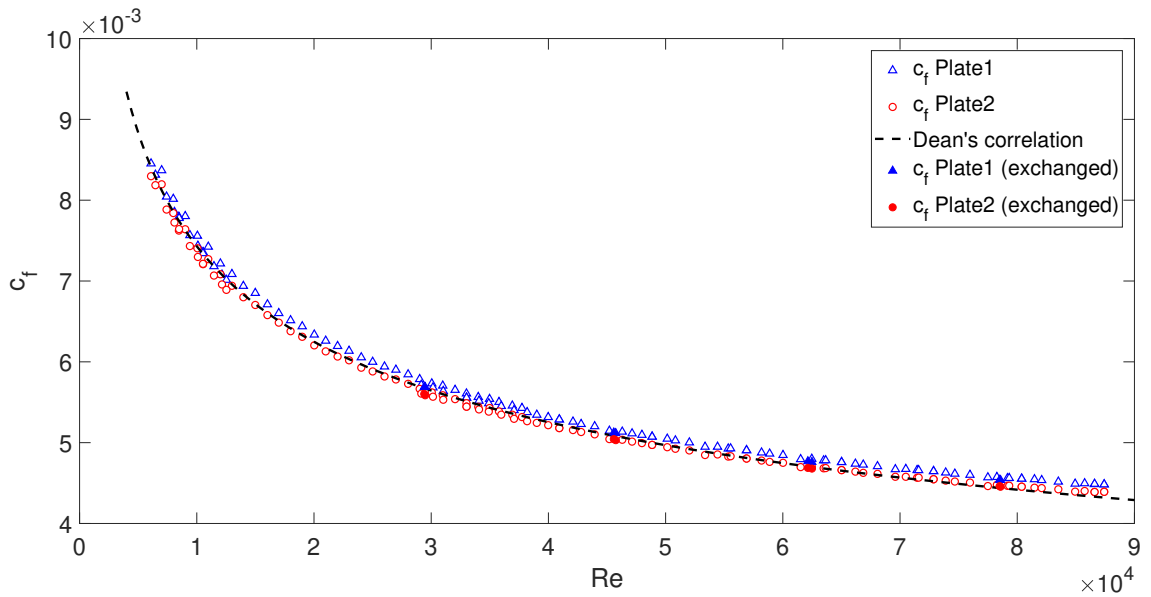


Figure 4.6: Plot of  $Re$ - $c_f$  relation separately for the two Plates positions Plate1 and Plate2. The Dean's correlatin is shown with a black dashed line. Filled points correspond to the measurements with exchanged plates.

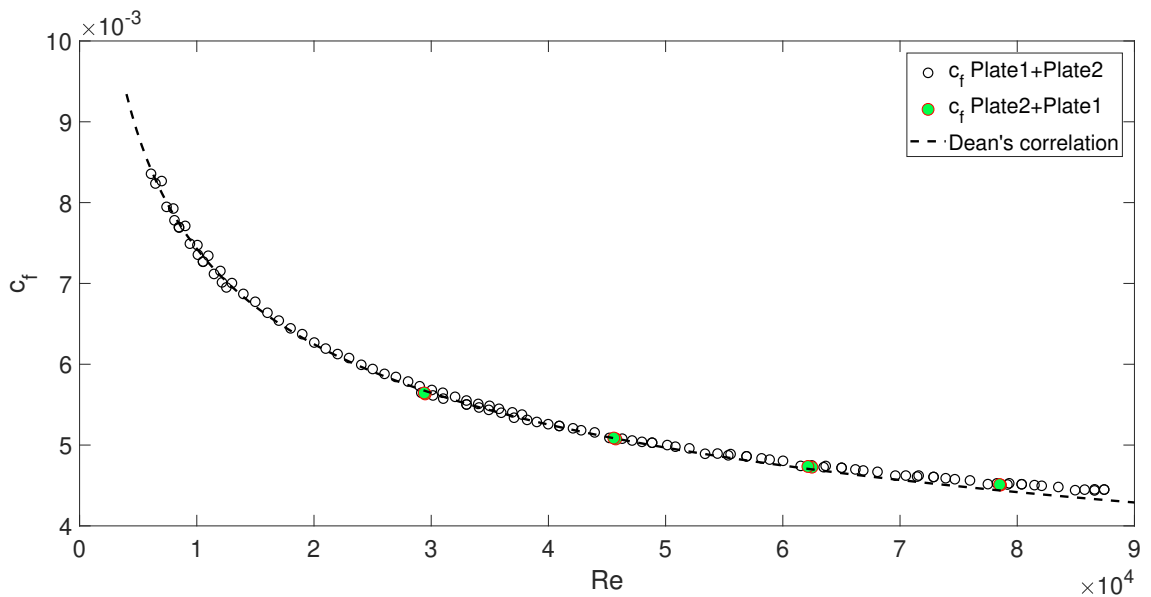


Figure 4.7: Plot of  $Re$ - $c_f$  relation for the entire test section. Green points correspond to the measurements of the skin friction when the plates position is inverted.

roughness has a minimal influence on the measurements. The main role is played by the taps selection in the post processing and by the error in the position of the same taps.

Finally, Figure A.4 shows the results calculated exploiting the entire test section, with no distinction between Plate1 and Plate2. In this case the wall pressure drop along the test section is calculated as the angular coefficient of the linear regression of the 13 available taps. In the graph, black circles correspond to the results of the measurement campaign, while green points come from the measurements with exchanged plates. All those points lie inside the uncertainty band calculated in Chapter 3. The perfect matching of the results obtained with exchanged plates with the ones obtained during the campaign, confirms the quality of the measurements taken with the smooth plates. This data set will be used as a smooth reference for the subsequent experiments with riblets.

## 4.4 Inlet Nozzle

A few measurements were also performed with the inlet nozzle as an instrument to measure the air mass flow rate running through the facility. The measurements were taken with the nozzle of bigger diameter, ...  $\mu m$ , in order to investigate the performance of this measurement instrument in the more critical area, namely for high Reynold numbers. The measurements are shown in Figure 4.8.

As in previous figures the skin friction coefficient was calculated separately for the two smooth plates. Accordingly to the measurements taken with the orifice meter, the same discrepancy between the  $c_f$  of the two plates is observed. Furthermore the trend of the measurements with the inlet nozzle appears not to be in line with the slope of the Dean's correlation. Consequently, only the measurements with the orifice meter, characterized by better quality, were considered for the smooth reference.

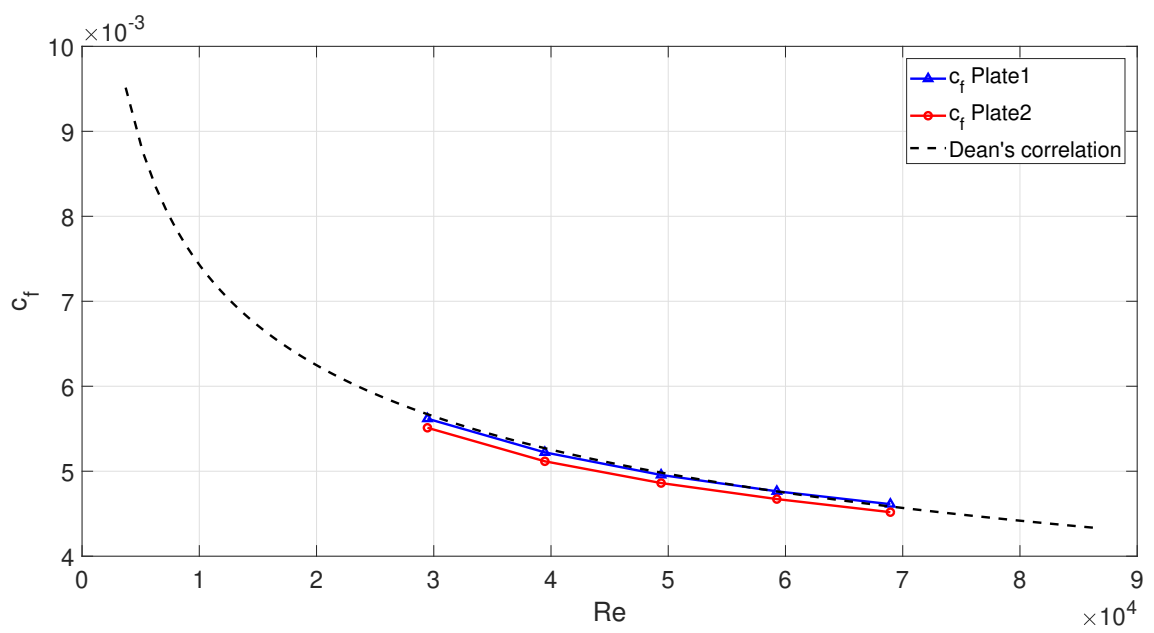


Figure 4.8: Skin friction coefficient measured when the inlet nozzle was used for the estimation of the flow rate.



# Chapter 5

## Riblets

In this Chapter is contained the core part of this thesis: the measurement of the skin friction reduction caused by riblets. They are protrusions of the surface aligned with the flow direction. Examples of riblet surfaces were found in nature, in the skin of fast-swimming sharks: those structures are aligned to the flow direction and contribute to the skin friction reduction in the turbulent flow regime. Another case of riblet surface was found in the beak of a bird (Rynchops), S.Martin and B.Bhushan (2016) [22], that catches fishes flying over the water surface and partially immersing the beak in water.

Many experimental studies attested their effectiveness both in laboratory and in full aerodynamic configurations. Riblets are passive drag reduction techniques, since they don't require momentum or energy source to perform their action. Tests in wind tunnels have been conducted on riblets of different geometries, evidencing a maximum drag reduction, over flat surfaces, of 10% (Bechert et al., 1997 [21]). Comparing the results from the different geometries, the blade-shaped riblets ensure the maximum performance, but those riblets are fragile and easily subject to cracks, in addition to being of difficult fabrication and maintenance. The fatigue behaviour, in HCF and VHCF, of scapolled riblets manufactured on thin sheets of high strength aluminum alloy was tested in the study of S. Stille, 2016 [24]. Three dimensional riblets, inspired to the discontinuous structures on shark skin, have been created and tested (Bechert et al., 1997 [21] and Bechert et al., 2000 [23]). However segmented-blade riblets, staggered between each row of blades, performed no gain in drag reduction with respect to continuous two-dimensional blade riblets.

In the recent years the success of riblets is increased and several technical applications have been found, including competition swimming suits and hull of sail boats for yacht races. Flight tests with aircrafts partially or completely covered with riblets were conducted (McClean et al., 1987 [26] and Viswanath, 2002 [25]), attesting a drag reduction of 2-3%.

## 5.1 Riblets mechanism of drag reduction

The physical principle behind the viscous drag reduction is the decrease of the cross-flow momentum transfer from the surface. This phenomenon is the basis of all the devices implemented for viscous drag reduction in turbulent flows. In fully developed turbulent flows, the motion of the molecules is assumed to be completely random, but some organized deterministic structures can be recognized in the near-wall turbulent dynamics: these structures create bursting motions. Secondary streamwise vortices form at the surface of the viscous sublayer. Those vortices both translate in the flow direction parallel to the surface and rotate, interacting with the wall and with other vortices. Consequently vortices are ejected from the near-wall region and enhance the momentum transfer in the cross-flow direction. The longitudinal vortices were observed with flow visualization techniques (Lee & Lee, 2001 [27]), reported in Figure 5.1, over smooth and ribleted surfaces.

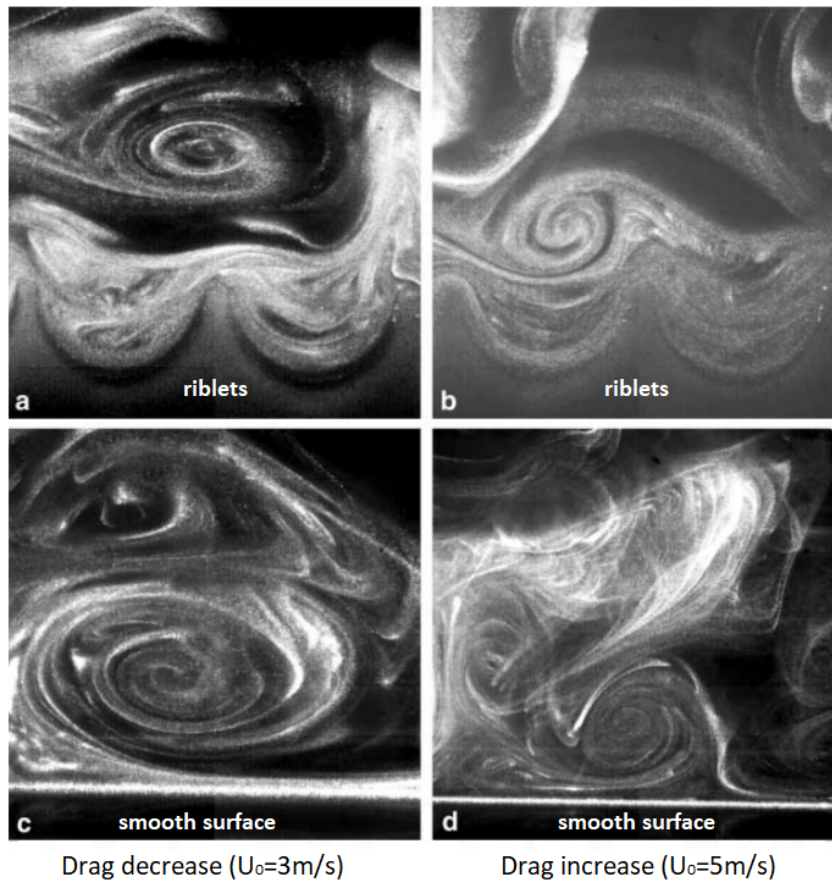


Figure 5.1: Vortex visualization in smooth and riblets surfaces at different velocities. (Lee & Lee, 2001 [27])

The mechanism of cross flow hampering of riblets is still not fully understood and argument of scientific debate. Figure 5.1 suggests that the riblets shift the axis of the streamwise vortices away from the surface. Those vortices now only interact with the tips of the riblets and hamper the momentum transfer from the rib valleys. As a consequence the increase in wetted surface area, caused by the introduction of riblets with respect to smooth surface, is counteracted by the low fluid speed in the riblet valleys, characterized by lower shear stress. Riblets of appropriate dimension diminish the cross-flow fluctuations and the momentum transfer near the surface, despite of the increase in wetted area.

The riblets are effective in modifying the flow as above described, only if they are immersed in the viscous sublayer of the flow boundary layer. The thickness of the viscous sublayer varies depending on the viscosity of the fluid and on the Reynolds number. For this reason the dimension of the riblets must be adapted to the particular application, considering the range of velocities in which the maximum drag reduction is required.

Furthermore, prediction on the riblets behaviour can be based on the analysis of the protrusion height: the difference between the riblet tip and the virtual origin of the velocity profile in the near-wall region. A visualization of the protrusion height in the longitudinal and crossflow direction  $s$  reported in Figure 5.2. At low Reynolds numbers  $s^+$  the difference between these two quantities  $\Delta h = h_{pl} - h_{pc}$ , normalized by the rib spacing  $s$ , is proportional to the drag reduction. One relation between the protrusion height and the drag reduction in the viscous flow regime is proposed in the following Section.

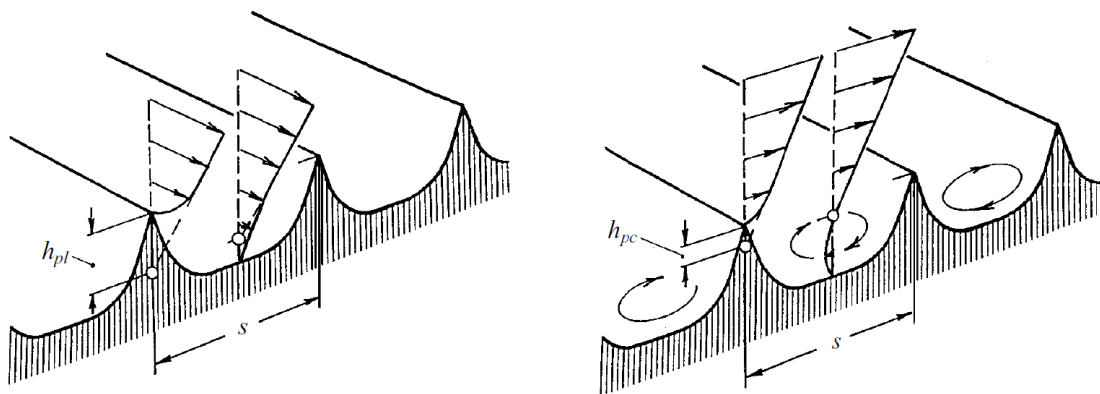


Figure 5.2: Longitudinal and crossflow protrusion height. (Bechert et al., 1997 [21])

## 5.2 Results

The second measurement campaign was conducted to investigate the effects of drag reduction obtained with riblets. Experiments have been conducted with three sets of plates with riblets of different dimensions. Consequently the optimum performance is obtained for different values of Reynolds number for the three analyzed sets. The ribleted plates were positioned in the last part of the test section, close to the outlet, while the first part of the test section was kept in the same conditions of smooth wall. The dimensions of the ribleted plates were not sufficient to cover the entire internal surface of the test section. This setup was chosen to ensure that the riblets were invested by a fully developed turbulent flow. Additionally, the measure of the static pressure drop in the first taps of the test section, where the smooth plates were kept, allows to compare the measurements with the previous ones, used as a reference to evaluate the entity of the drag reduction (see Chapter 4). The comparison of this two data sets is a good monitoring instrument for the good reproducibility of the skin friction coefficient measurement. In each of the three following sections are reported the geometrical features of one of the tested ribleted plates and the corresponding results.

The drag reduction will be expressed through the ratio  $\Delta\tau/\tau_0$ , where  $\Delta\tau = \tau - \tau_0$  is the difference between the wall shear stress of the ribleted plate  $\tau$  and the wall shear stress of the smooth reference plate  $\tau_0$ . Considering the sign of  $\Delta\tau$  it is immediately possible to understand the effect of the structured surface causes a drag reduction (negative) or a drag increase (positive) with respect to the smooth reference. The parameter  $\Delta\tau/\tau_0$  will be expressed as a function of the Reynolds number for the riblets

$$s^+ = \frac{su_\tau}{\nu}$$

where the characteristic length is the lateral rib spacing  $s$  and the velocity is defined as  $u_\tau = (\tau_0/\rho)^{\frac{1}{2}}$ .

The relevant parameter that can be related to the hampering of the crossflow in the near wall region, as already mentioned in the previous section, is  $\Delta h$ , that is the difference between the longitudinal and crossflow protrusion height. For low values of Reynolds number, the fluid has a basically viscous interaction with the ribs. In this region the wall shear stress difference  $\Delta\tau/\tau_0$  linearly increases with increasing  $s^+$ . A connection between the protrusion height difference and the drag reduction in the viscous regime was found by Luchini (1992) [20] and appears for the first time in a scientific journal in the article of Bechert (1997) [21].

$$\frac{\Delta\tau}{\tau_0} = \frac{0.785(\Delta h/s)}{(2c_f)^{-1/2} + 1.25} s^+ = VRC \cdot s^+$$

In the same article it is reported the result from the analytical calculation of the protrusion height difference as a function of the riblet geometry and shape. This results are contained in Figure 5.3.

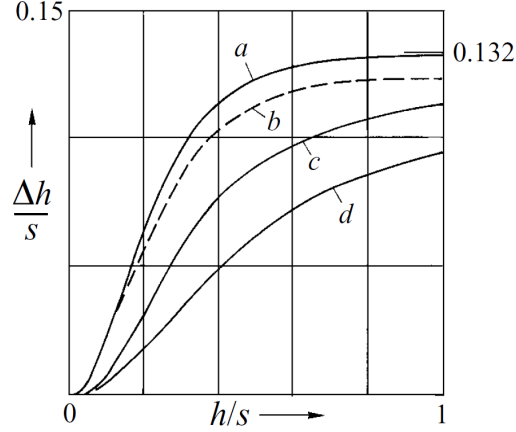


Figure 5.3: Protrusion height as a function of the geometry, for different riblets configurations: (a) blade riblets, infinitely thin, (b) blade riblets, blade thickness 2% of lateral rib spacing, (c) parabolic groove profile, (d) triangular riblets (taken from [21]).

The results will be subsequently shown for riblets of progressively reduced rib spacing  $s$ .

### 5.2.1 Riblet set I

The first analyzed set of ribletted plates was manufactured at the RWTH of Aachen with appositely built diamond machining tools. The riblets of trapezoidal shape were machined by chip removal on a plastic plate in an area of 300x1500 mm. To ensure the structural rigidity of the plates, they were fixed on a steel component of the same dimensions. This plates were manufactured with an extremely high accuracy and their dimensions are reported in Figure 5.4. The riblets design ensures that the cross sectional area of the test section keeps equal to the one of the smooth reference case.

The skin friction coefficient measured on the rib surface is shown in Figure 5.5. In the same graph those results are compared with the smooth reference measured in the same taps covered by the ribletted plate, which correspond to the plate closer to the outlet of the test section (red circles in Figure 4.6). Comparing the skin friction coefficient of the smooth and ribletted plates it's possible to observe a drag reduction until  $Re = 19000$ . For higher values of  $Re$  the riblets are not effective and the increase of wetted surface causes a drag increase with respect to the smooth

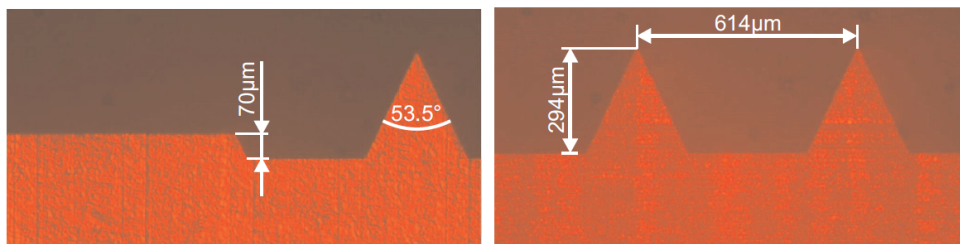


Figure 5.4: Cross sectional view on trapezoidal riblets manufactured at RWTH Aachen. For additional information refer to [1].

reference. However, in this plot it is difficult to find the Reynolds number at which the maximum drag reduction occurs. To have a better view of this point, as introduced in the initial part of this section, the normalized wall shear stress difference have been plotted as a function of the riblets Reynolds number in Figure 5.6. The best performance of the riblets is obtained at  $s^+ = 15$  ( $Re = 11700$ ), with a drag reduction of 6% with respect to the smooth reference.

Both plots evidence a good matching between the results obtained with the 60 mm and the 105 mm orifice. Those results are in good agreement with the ones of Güttler 2015 [1].

Finally, the prediction of the drag reduction in the viscous region is hard to be applied for trapezoidal riblets. In fact, for this riblet shape, no analytical calculations have been found for the correlation between the protrusion height and the rib geometry. From the comparison of different analytical calculations of  $h_{pc}$ , it appears that this parameter is around constant and independent from the riblets geometry. Consequently, the yellow line in Figure 5.6 was obtained reading the value of  $h_{pl}$  from the prediction for trapezoidal riblets present in Bechert *et al.* 1997 [21] and taking  $h_{pc}$  equal to the value predicted by Luchini, shown in the same scientific article. The slope of the Bechert correlation, derived with this assumptions, matches quite well with the measured behavior of the trapezoidal riblets in the viscous regime. Moreover there is a good continuity between the measurements of the orifice of different diameter.

The results obtained from the measurements on this riblet plates are summarized in table 5.1. The VCR was calculated considering the maximum and the minimum measured skin friction coefficient in the ribletted plates. The value of the VCR selected for the line represented in Figure 5.6 was obtained with the mean value of measured  $c_f$ .

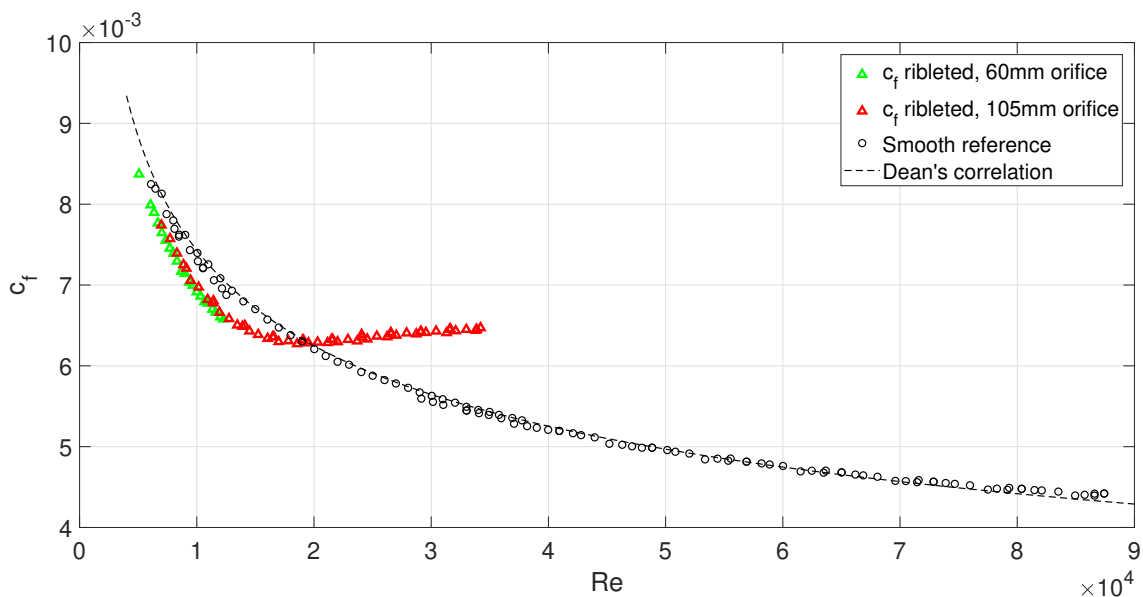


Figure 5.5: Skin friction coefficient measured for the trapezoidal riblets surface, compared with the smooth reference.

Shape	Plate length [mm]	$s_{opt}^+$	$\Delta\tau/\tau_{0,max}$	VRC
trapezoidal	1500	15	-6%	(0.50; 0.59)

Table 5.1: Features of the trapezoidal riblets set. The VRC was calculated with the assumption of sawtooth riblets.

### 5.2.2 Riblet set II

The second set of analyzed ribletted plates was obtained gluing a plastic sheet, manufactured by the company 3M, on a steel plate of dimensions 1100x350 mm and thickness of 10 mm. The dimensions of the layer and of the riblets are reported in Figure 5.7. The steel plates were machined in the part destined to gluing, to preserve an equal the cross sectional area of the test section.

However the manufacturing accuracy was lower with respect to the first analyzed ribletted plate and some discontinuity of the gluing was caused by air bubbles trapped between the plastic layer and the steel plate. Furthermore the shorter plate dimensions limited the number of possible considered pressure taps to 6. Consequently the taps considered in the post processing of the smooth reference data was reduced to the same taps. The results of the measurements of the skin friction coefficient are reported in Figure 5.8. The different colors in this graphs represent measurements

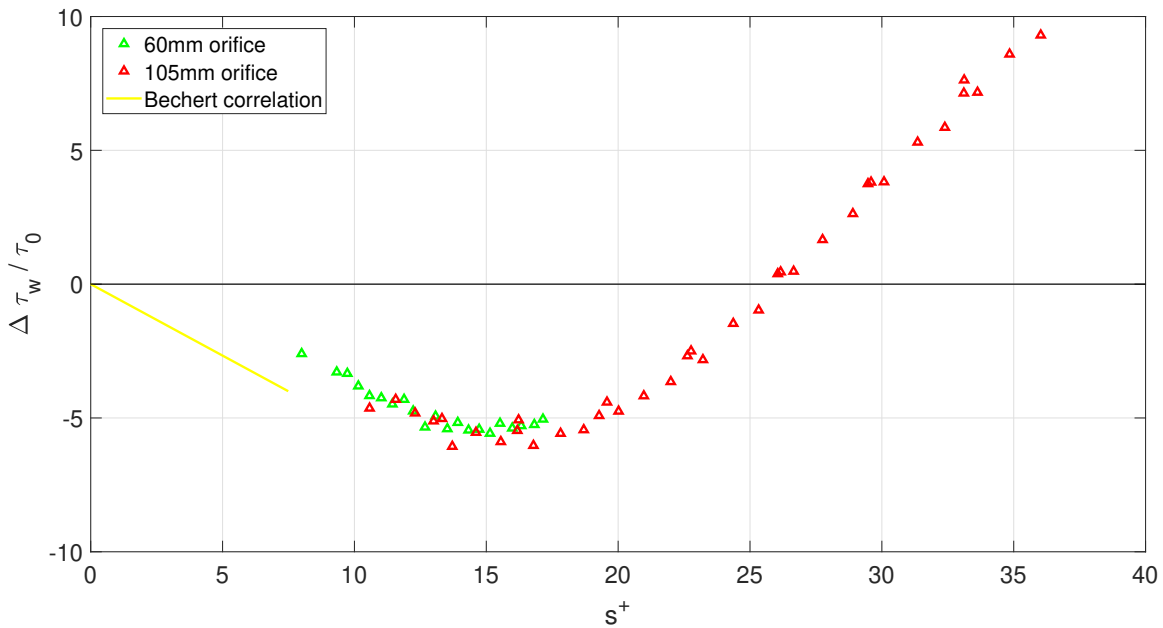


Figure 5.6: Plot of the wall shear stress difference, for trapezoidal riblets, depending on the riblets Reynolds number. The yellow line is the Bechert correlation in the viscous regime.

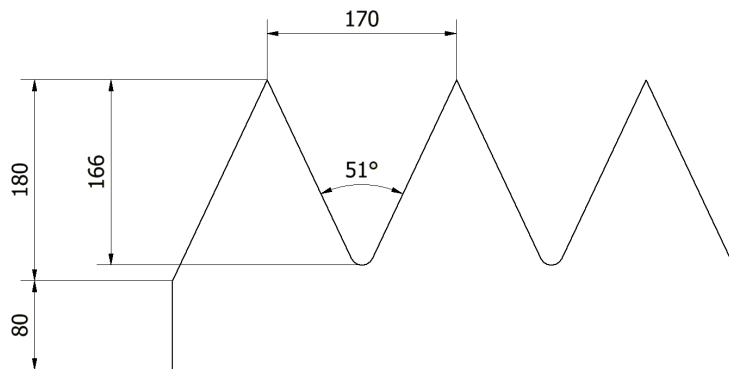


Figure 5.7: Sketch of the sawtooth shape riblets with spacing  $s = 170 \mu m$ , manufactured by 3M. All the dimensions are expressed in  $\mu m$ .

with different orifices. An evident discontinuity between the results from  $105 \mu m$  and  $150 \mu m$  can be observed.

A correspondent step is present in Figure 5.9, where the difference in the wall

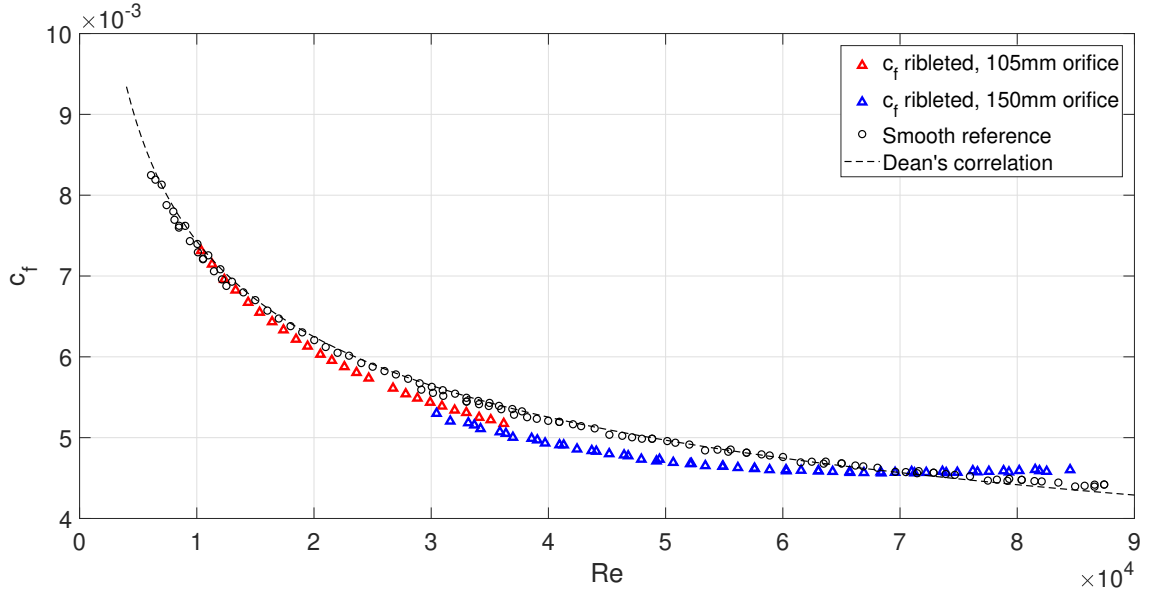


Figure 5.8: Skin friction coefficient measured for the sawtooth riblets surface with rib spacing  $s = 170 \mu m$  compared with the smooth reference.

shear stress is represented. This step is due to the measure of the air flow rate, that presents a systematic difference with the reference measurement. This change was found comparing the measurements in the smooth plate positioned closer to the inlet of the test section, taken for the smooth reference and for the case of riblets. It was clear that the measurements with the  $105 \mu m$  orifice were well reproduced, but the results with the  $150 \mu m$  orifice were shifted with respect to the smooth reference. The measurements were repeated and several attempts were made to get a better reproducibility, but the same shift was observed every time. Nevertheless the Bechert prediction for the viscous region, that can be observed in the same Figure, is in line with the slope of the experimental measurements.

Finally, the Table 5.2 is a summary of the main properties of this riblets set.

Shape	Plate length [mm]	$s_{opt}^+$	$\Delta\tau/\tau_{0max}$	VRC
triangular	1100	15	-6%	(0.54; 0.67)

Table 5.2: Characteristics of the triangular riblets set with rib spacing  $s = 170 \mu m$ .

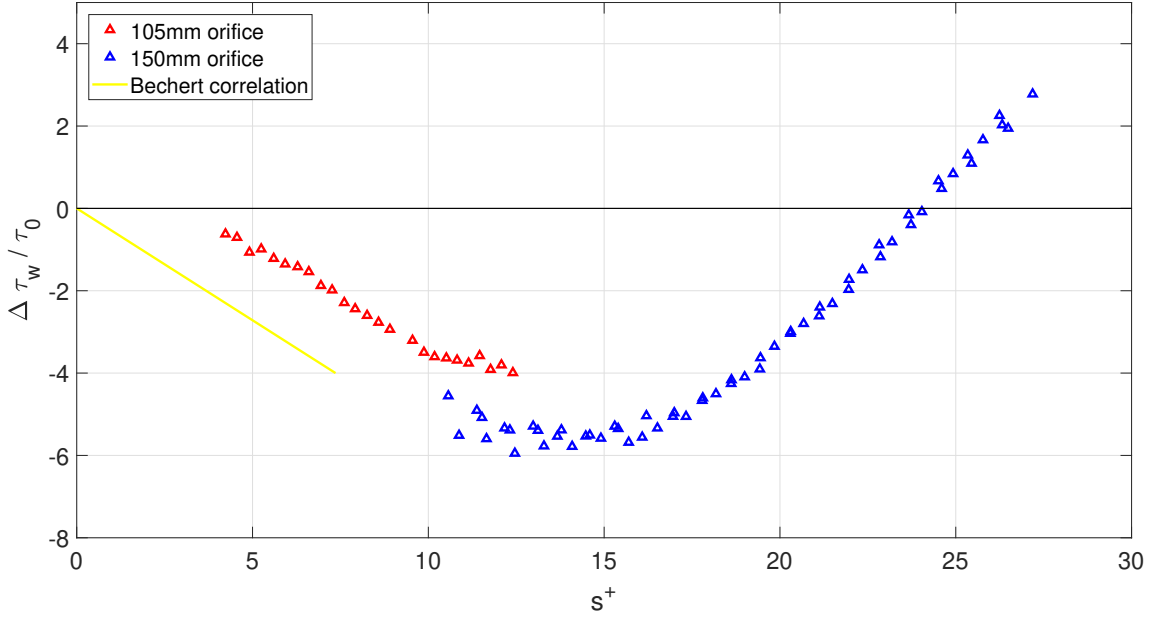


Figure 5.9: Plot of the wall shear stress difference, for sawtooth riblets with spacing  $s = 170 \mu m$ , depending on the riblets Reynolds number. The yellow line is the Bechert correlation in the viscous regime.

### 5.2.3 Riblet set III

The last set of riblets to be tested presented the geometrical features reported in Figure 5.10. As in the previous case, the riblets were manufactured by the company 3M as plastic sheet, that have been glued to a steel plate. The dimension of the plates covered the same taps as in the second analyzed riblets set. The same adjustment were adopted in the calculations. Air bubbles trapped during the gluing and lower quality of the ribletted surface with respect to the first riblets set were observed.

The structure and the reported graph are the same as in the previous Sections. For this reason the results will be directly commented.

The small riblets spacing  $s$  shifts the optimal efficiency of this riblets set to higher values of Reynolds number. The facility is designed for low Reynolds number testing and does not allow to reach this point. However observing Figure 5.12 the maximum performance of the riblets can be estimated at around  $Re = 90000$ .

A shift between the results from the two orifices was reproduced also in this case, but the Bechert prediction is in line with the experimental measurements. The comparison of the results from the smooth plate allow to state that the shift is systematic and with the same value as in the previous case.

Moreover, the maximum drag reduction measured with this riblets set is around

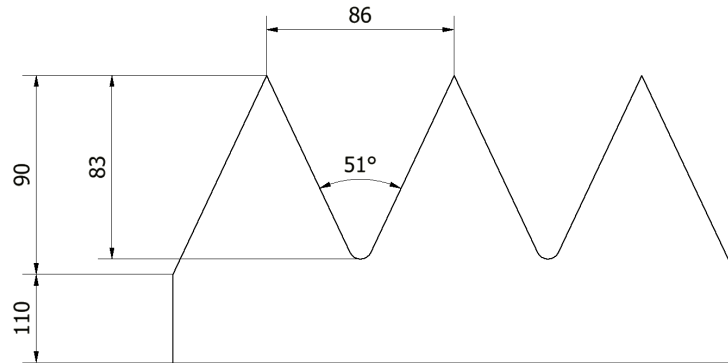


Figure 5.10: Sketch of the sawtooth shape riblets with spacing  $s = 86 \mu m$ , manufactured by 3M. All the dimensions are expressed in  $\mu m$ .

8%. It is inconsistent with the results obtained with the previous ribletted surfaces and with the results in literature. Instead the shape of the wall shear stress difference in Figure 5.12 is in line with the typical behaviour of the riblets.

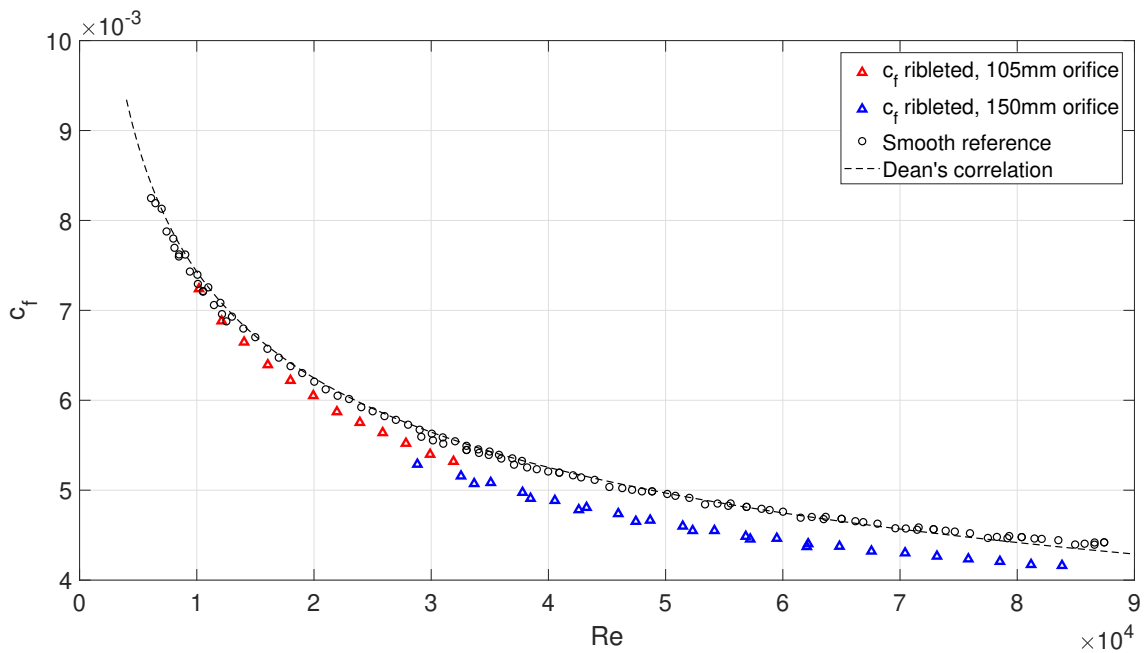


Figure 5.11: Skin friction coefficient measured for the sawtooth riblets surface with rib spacing  $s = 86 \mu m$  compared with the smooth reference.

Consequently the excessive measured drag reduction could be attributed to the

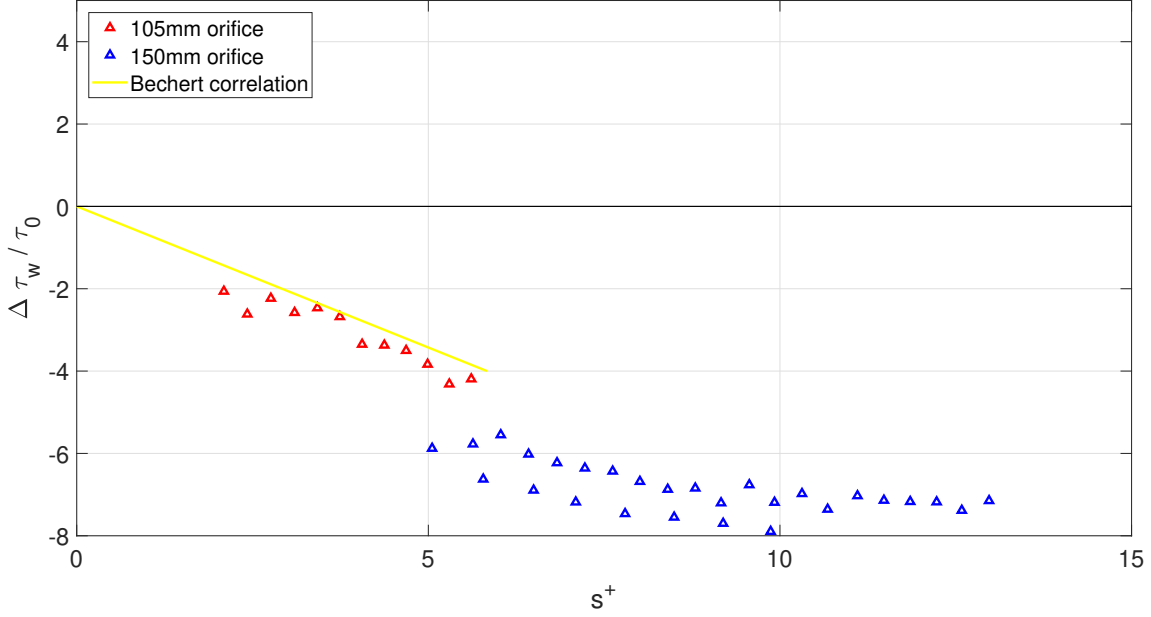


Figure 5.12: Plot of the wall shear stress difference, for sawtooth riblets with spacing  $s = 86 \mu m$ , depending on the riblets Reynolds number. The yellow line is the Bechert correlation in the viscous regime.

Shape	Plate length [mm]	$s_{opt}^+$	$\Delta\tau/\tau_{0,max}$	VRC
triangular	1100	15	-8%	(0.56; 0.71)

Table 5.3: Characteristics of the sawtooth riblets set with rib spacing  $s = 86 \mu m$ .

modification of the test section cross sectional area caused by this particular ribletted plates. A reduction of the cross section would lead to higher speeds, higher pressure drops along the test section and lower calculated skin friction coefficients.

# Chapter 6

## conclusions

The present Master's Thesis work deals with high accuracy measurements of the skin friction reduction achieved with riblets, in a fully developed turbulent air flow. In the first part, pressure sensors have been calibrated in the best possible way: the less accurate sensors, involved in the flow rate measurement, have been calibrated by aligning their characteristic to the one of the high accuracy sensor, involved in the static pressure drop measurement.

As a preliminary analysis, the uncertainty of the wind tunnel facility was estimated with the Taylor Series Method. The uncertainty, both in the air flow rate and in the skin friction coefficient measurement, showed results comparable with the previous analysis, on the same facility, calculated by Güttler 2015 [1] exploiting the linear error propagation.

Subsequently the skin friction coefficient for a smooth surface have been successfully measured in the range of Reynolds numbers  $7 \cdot 10^3 < Re_b < 87 \cdot 10^4$ : the lower boundary of this interval is imposed by the requirement of fully developed turbulent flow, while the upper limit is fixed by the full-scale value of the pressure sensors. Particular investigations have been carried to understand the effects of the main parameters on the measurement. The further polishing of the smooth plates have been proved to have a negligible influence on the measurements. The temperature of the air flowing through the wind tunnel have been monitored through the use of thermocouples and the initial settling time have been defined. The most important parameter to be controlled is the compressibility of air, that strongly influences the measurements at high Reynolds numbers. A correction, that takes into account the relation between the fluid velocity and density, have been introduced in data post processing. The final results of the smooth skin friction coefficient present a very high accuracy and a good match with the data in literature. Additional measurements of the smooth surface skin friction have been taken with a modified setup for the flow rate measurement: the orifice meter, exploited for the aforementioned flow rate measurements, was replaced with an inlet nozzle. Those results exhibited

a lower accuracy and were not included in the set of data exploited to generate the smooth reference.

In the second part of the measurements, three sets of riblets were tested and compared to the smooth reference to calculate the percentage of wall shear stress reduction. The results exhibited a maximum wall shear stress reduction of 5 – 8%. The well known curve that relates the wall shear stress reduction and the non dimensional wall spacing was successfully reproduced in all the tests. A further confirmation of the quality of the measurements is the Luchini correlation in the viscous regime, that finds a good match with the experimental measurements.

However the measurements involving the orifice meter of diameter 150 *mm* were characterized by a step, considerably larger than in the smooth reference, in correspondence of the transition range between the two orifices. This step was repeatably measured and was present both in the riblets measurements and in new measurements taken with the smooth surface.

An outlook for the future developments of this Master's Thesis, is first related to the correction of the registered step: new measurements for the smooth reference must be taken with the 150 *mm* orifice meter and new calculations of the wall shear stress reduction have to be performed. Furthermore the agreement between orifice measurements should be improved by calibrating them through the use of a more precise instrument: a possible solution is to exploit a Coriolis mass flow meter with high accuracy.

ISTM is currently working to equip the wind tunnel with new components and technologies, in order to perform different measurements. In the next years, a deeper insight into the skin friction reduction mechanism of riblets will be achieved through hot wire measurements, plasma actuators and flow visualization techniques.

# Appendix A

## Hot wire measurements

Hot wire measurements were performed on the turbulent flow close to the exit of the test section. This technique relates the temperature and resistivity of a wire immerse in a fluid to the velocity of the flow, through a heat exchange balance. The hot wire anemometer consists of a wire that is heated by an electric current and is kept at the constant temperature. When the flow velocity increases, the heat loss of the wire correspondently increase and the measurement device increases the current through the wire. The wire very thin so that it has a negligible impact on the flow characteristics.

The focus of this measurements is to compare the flow velocity, in the near wall region, between the smooth and the ribletted surface. The position of the wire is controlled and measured with extreme precision through a positioning device, that allows movements in the two directions perpendicular to the flow direction.

The following graphs show the results of the measurements, taken in the middle section of the test section. The variables involved correspond to the velocity and the distance from the wall:

- $U$  : mean velocity
- $u$  : fluctuation component of velocity
- $U_d$  : center line velocity
- $y$  : distance from the wall
- $\delta$  : semiwidth of the test section
- $U^+$  : dimensionless velocity
- $y^+$  : dimensionless wall distance

The dimensionless coefficients are defined as follows:

$$y^+ = \frac{y u_\tau}{\nu}$$

$$u_\tau = \sqrt{\frac{\tau_w}{\rho}}$$

$$u^+ = \frac{u}{u_\tau}$$

The measurements show that riblets strongly reduce the fluctuation velocity component in the near wall region. This result is consistent to the wall shear stress coefficient reduction and confirms the drag reduction mechanism mentioned in Chapter 5.

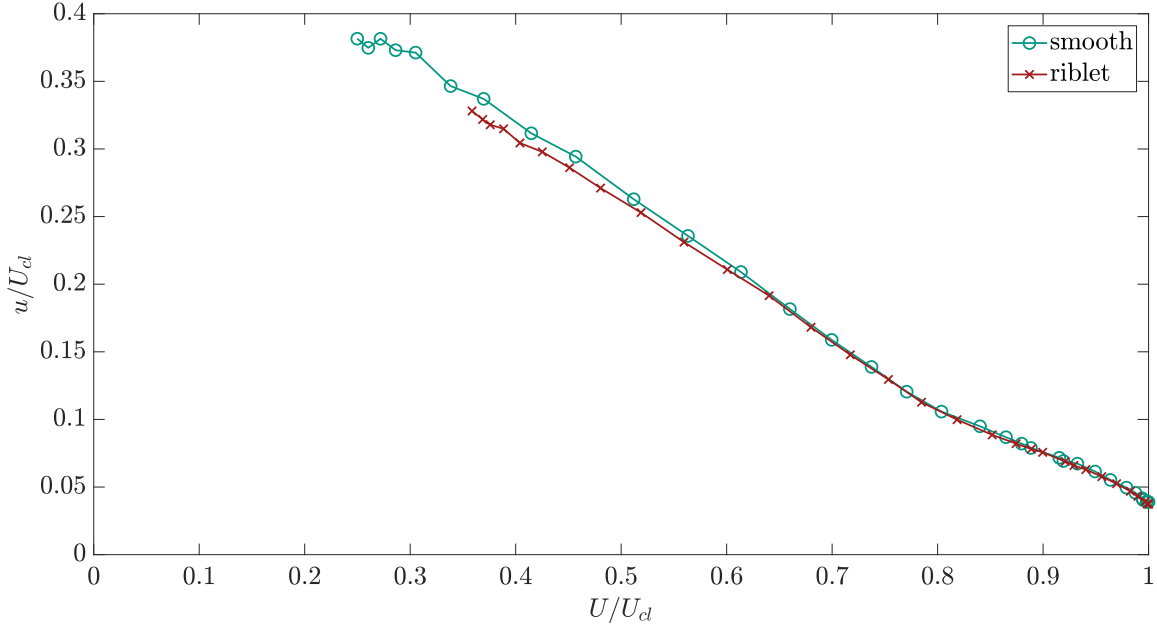


Figure A.1: Plot of the velocity fluctuation component related to the correspondent mean velocity component.

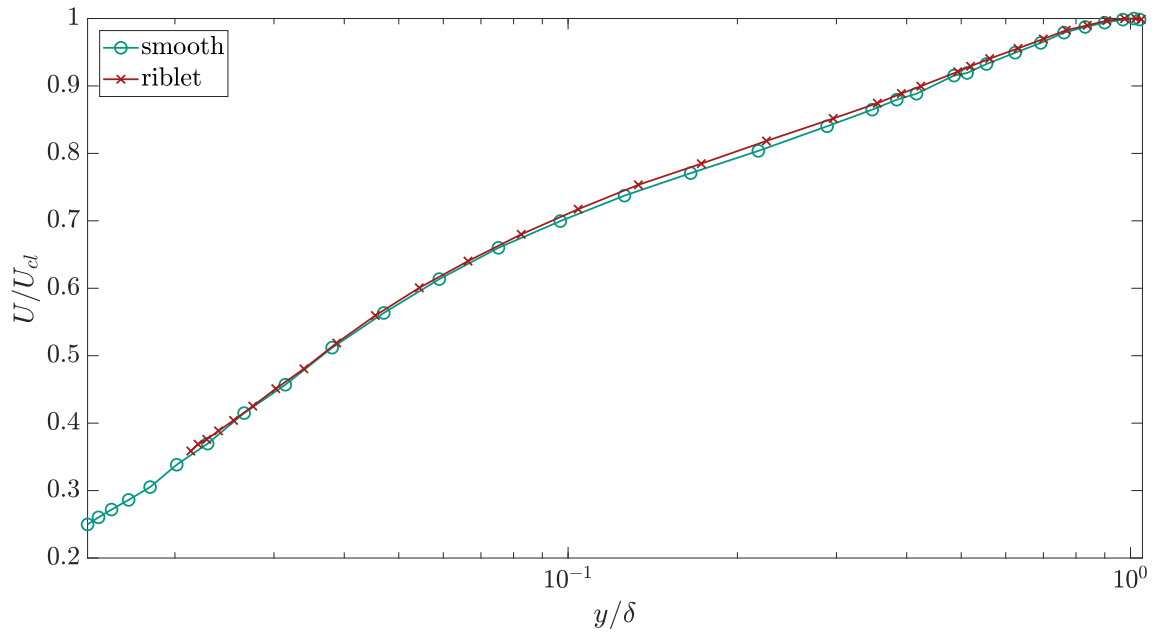


Figure A.2: Flow velocity measurement at different distances from the wall.

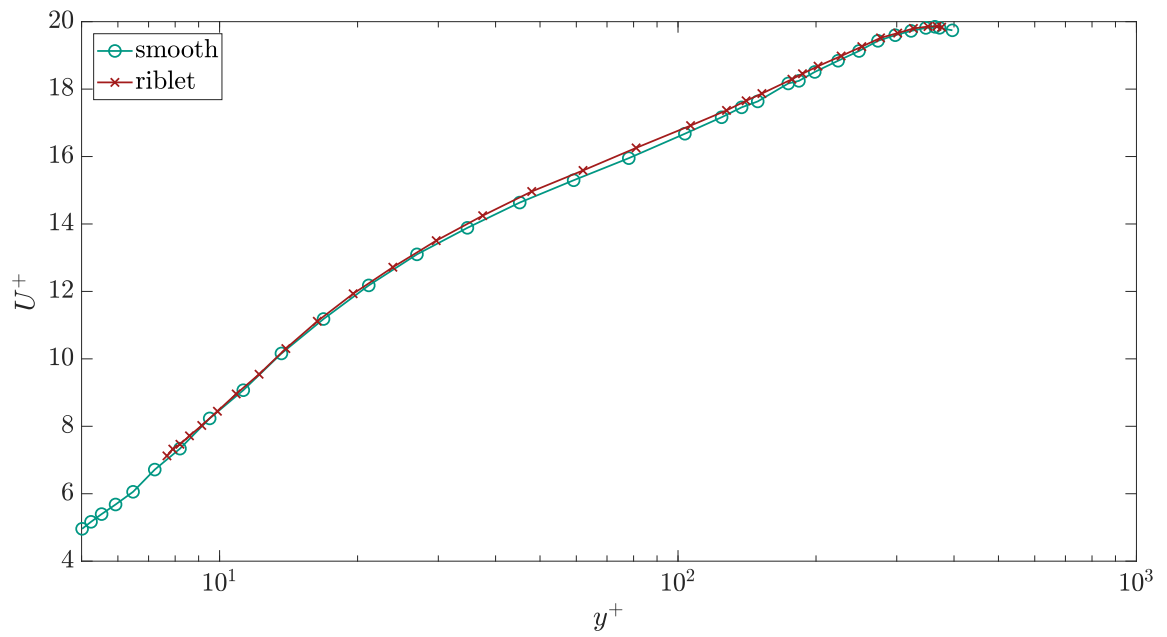


Figure A.3: Dimensionless flow velocity as a function of dimensionless wall distance.

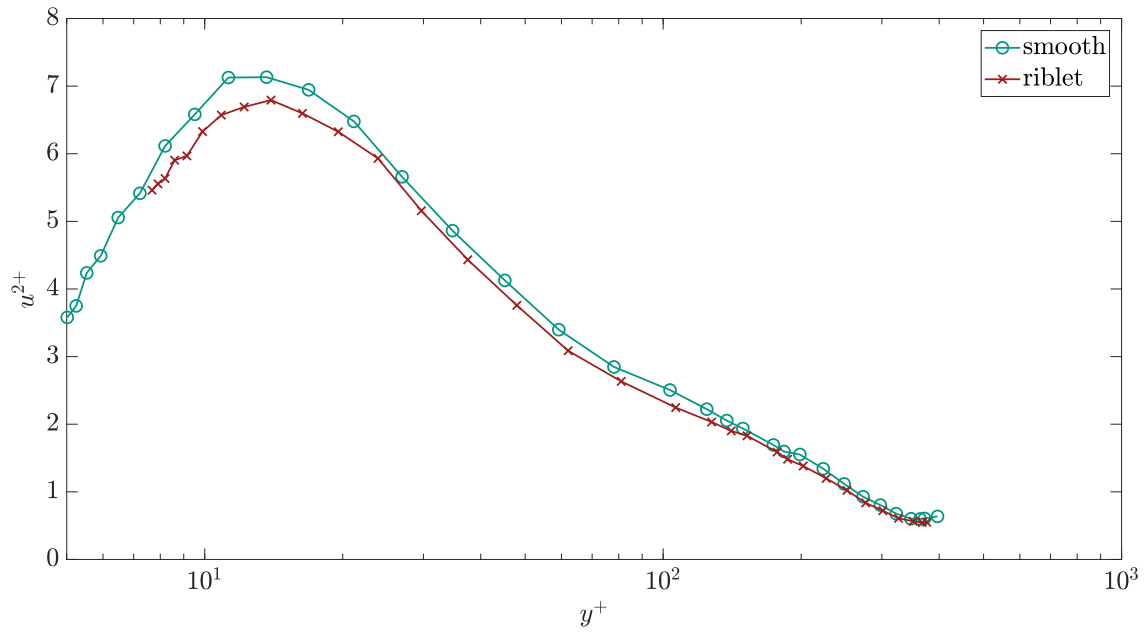


Figure A.4: Dimensionless velocity fluctuation as a function of the dimensionless wall distance.

# Bibliography

- [1] A. Güttler, *High accuracy determination of skin friction differences in an air channel flow based on pressure drop measurements*. KIT Scientific Publishing, 2015.
- [2] H. Jund, *Design, Aufbau und Test einer neuen Blendenmessstrecke*. (2017)
- [3] O. Cramer, *The variation of the specific heat ratio and the speed of sound in air with temperature, pressure, humidity, and CO<sub>2</sub> concentration* The Journal of the Acoustical Society of America 93.5 (1993): 2510-2516.
- [4] R. S. Davis, *Equation for the determination of the density of moist air (1981/91)*. Metrologia 29.1 (1992): 67.
- [5] J. Nikuradse, *Laws of flow in rough pipes*. National Advisory Committee for Aeronautics. NACA Technical Memorandum, NACA Technical Memorandum 1292 (1933): 60-68.
- [6] C. F. Colebrook, *Experiments with fluid friction in roughened pipes*. Proc. R. Soc. Lond. A 161.906 (1937): 367-381.
- [7] L. F. Moody, *Friction factors for pipe flows*. Trans. Asme 66 (1944): 671-684.
- [8] P. Bradshaw, *A note on critical roughness height and transitional roughness*. Physics of Fluids 12.6 (2000): 1611-1614.
- [9] A. A. Townsend, *The Structure of Turbulent Shear Flow*, 2nd edn. Cambridge University Press (1976).
- [10] J. J. Allen, et al., *Turbulent flow in smooth and rough pipes*. Philosophical Transactions of the Royal Society of London A: Mathematical, Physical and Engineering Sciences 365.1852 (2007): 699-714.
- [11] M. P. Schultz, and K. A. Flack, *The rough-wall turbulent boundary layer from the hydraulically smooth to the fully rough regime*. Journal of Fluid Mechanics 580 (2007): 381-405.
- [12] GrÃ¼neberger, RenÃ©, and Wolfram Hage. Drag characteristics of longitudinal and transverse riblets at low dimensionless spacings. Experiments in Fluids 50.2 (2011): 363-373.
- [13] Walsh, Michael J. "Riblets." Viscous drag reduction in boundary layers (1990): 203-261.
- [14] J. JimÃ©nez, *Turbulent flows over rough walls*. Annu. Rev. Fluid Mech. 36 (2004):

- 173-196.
- [15] R. B. Dean, *Reynolds number dependence of skin friction and other bulk flow variables in two-dimensional rectangular duct flow*. Journal of Fluids Engineering 100.2 (1978): 215-223.
  - [16] Coleman, Hugh W., and W. Glenn Steele. *Experimentation, validation, and uncertainty analysis for engineers*. John Wiley & Sons, 2018.
  - [17] Walsh, M. Turbulent boundary layer drag reduction using riblets. 20th aerospace sciences meeting. 1982.
  - [18] ISO, EN. Durchflussmessung von Fluiden mit Drosselgeräten in voll durchströmten Leitungen mit Kreisquerschnitt Teil 1: Allgemeine Grundlagen und Anforderungen (ISO 5167-1: 2003). Deutsche Fassung EN ISO 5167-1: 2003 (2003).
  - [19] DIN, ENISO. 5167-2: Durchflussmessung von Fluiden mit Drosselgeräten in voll durchströmten Leitungen mit Kreisquerschnitt-Teil 2: Blenden (ISO 5167-2: 2003). Deutsche Fassung EN ISO (2003): 5167-2.
  - [20] P. Luchini Effects of riblets on the growth of laminar and turbulent boundary layers. 7th European Drag Reduction Meeting. 1992.
  - [21] D. W. Bechert et al. Experiments on drag-reducing surfaces and their optimization with an adjustable geometry. Journal of fluid mechanics 338 (1997): 59-87.
  - [22] S. Martin and B. Bhushan. Discovery of riblets in a bird beak (Rynchops) for low fluid drag. Phil. Trans. R. Soc. A 374.2073 (2016): 20160134.
  - [23] D. W. Bechert, M. Bruse, and W. Hage. Experiments with three-dimensional riblets as an idealized model of shark skin. Experiments in fluids 28.5 (2000): 403-412.
  - [24] S. Stille, T. Beck, and L. Singheiser. Fatigue behavior of riblet structured high strength aluminum alloy thin sheets at very high cycle numbers. Key Engineering Materials. Vol. 664. Trans Tech Publications, 2016.
  - [25] P. R. Viswanath. Aircraft viscous drag reduction using riblets. Progress in Aerospace Sciences 38.6-7 (2002): 571-600.
  - [26] J. MCLEAN, D. E. Z. S. O. N. GEORGE-FALVY, and P. SULLIVAN. Flight-test of turbulent skin-friction reduction by riblets. Turbulent drag reduction by passive means (1987): 408-424.
  - [27] S-J. Lee and S-H. Lee. Flow field analysis of a turbulent boundary layer over a riblet surface. Experiments in fluids 30.2 (2001): 153-166.
  - [28] Dean, Brian, and Bharat Bhushan. Shark-skin surfaces for fluid-drag reduction in turbulent flow: a review. Philosophical Transactions of the Royal Society A: Mathematical, Physical and Engineering Sciences 368.1929 (2010): 4775-4806.
  - [29] Radmanesh, Mohammadreza, et al. Experimental study of square riblets effects on delta wing using smoke visualization and force measurement. Journal of Visualization 21.3 (2018): 421-432.

